

## Methane on the temperate exo-Saturn TOI-199 b

AARON BELLO-ARUFE  <sup>1</sup>, RENYU HU  <sup>1, 2, 3, 4</sup>, MANTAS ZILINSKAS  <sup>1</sup>, JEEHYUN YANG  <sup>5, 1</sup>, ARMEN TOKADJIAN  <sup>1</sup>,  
 LUIS WELBANKS  <sup>6</sup>, GUANGWEI FU  <sup>7</sup>, MICHAEL GREKLIK-MCKEON  <sup>8</sup>, MARIO DAMIANO  <sup>1</sup>,  
 JONATHAN GOMEZ BARRIENTOS  <sup>9</sup>, HEATHER A. KNUTSON  <sup>9</sup>, DAVID K. SING  <sup>10, 7</sup> AND XI ZHANG  <sup>11</sup>

<sup>1</sup>Jet Propulsion Laboratory, California Institute of Technology, Pasadena, CA 91109, USA

<sup>2</sup>Department of Astronomy & Astrophysics, The Pennsylvania State University, University Park, PA 16802, USA

<sup>3</sup>Center for Exoplanets and Habitable Worlds, The Pennsylvania State University, University Park, PA 16802, USA

<sup>4</sup>Institute for Computational and Data Science, The Pennsylvania State University, University Park, PA 16802, USA

<sup>5</sup>The University of Chicago, Chicago, IL 60637, USA

<sup>6</sup>School of Earth and Space Exploration, Arizona State University, 781 Terrace Mall, Tempe, AZ 85287, USA

<sup>7</sup>Department of Physics & Astronomy, Johns Hopkins University, Baltimore, MD 21218 USA

<sup>8</sup>Earth and Planets Laboratory, Carnegie Institution for Science, Washington, DC 20015, USA

<sup>9</sup>Division of Geological and Planetary Sciences, California Institute of Technology, Pasadena, CA 91125, USA

<sup>10</sup>Department of Earth & Planetary Sciences, Johns Hopkins University, Baltimore, MD 21218, USA

<sup>11</sup>Department of Earth and Planetary Sciences, University of California Santa Cruz, Santa Cruz, CA 95064, USA

## ABSTRACT

Temperate ( $T_{\text{eq}} < 400$  K) gas giants represent an unexplored frontier in exoplanet atmospheric spectroscopy. Orbiting a G-type star every  $\sim 100$  days, the Saturn-mass exoplanet TOI-199 b ( $T_{\text{eq}} = 350$  K) is one of the most favorable low-temperature gas giants for atmospheric study. Here, we present its transmission spectrum from a single transit observed with JWST’s NIRSpec G395M mode. Despite lower-than-nominal precision due to a pointing misalignment, Bayesian retrievals reveal the presence of CH<sub>4</sub> (Bayes factor of  $\sim 700$  in a cloudy atmosphere), corresponding to a metallicity of C/H =  $13^{+78}_{-12} \times$  solar, although the absence of detectable CO and CO<sub>2</sub> disfavors metallicities  $\gtrsim 50 \times$  solar. We also tested several haze prescriptions (Titan-like tholin, soot, and water-rich tholin), but the preference for these models is weak (Bayes factors of  $\sim 2$  relative to the clear case). The spectrum also shows an increase in transit depth near 3  $\mu\text{m}$ , which our self-consistent models attribute to either NH<sub>3</sub> or, less likely, HCN. Follow-up observations will distinguish between these species, helping determine the planet’s vertical mixing regime. The TOI-199 system exhibits strong transit timing variations (TTVs) due to an outer non-transiting giant planet. For planet c, our TTV analysis reduces its mass uncertainty by 50% and prefers a slightly longer orbital period (still within the conservative habitable zone) and higher eccentricity relative to previous studies. TOI-199 b serves as the first data point for studying clouds and hazes in temperate gas giants. The detection of methane supports the emerging trend that temperate low-molecular-weight atmospheres display spectral features in transmission.

**Keywords:** Exoplanet atmospheric composition (2021) — Extrasolar gaseous giant planets (509) — G dwarf stars (556) — James Webb Space Telescope (2291) — Transit timing variation method (1710) — Transmission spectroscopy (2133)

## 1. INTRODUCTION

Hot Jupiters have dominated the landscape of atmospheric studies of exoplanets over the past two decades. Their frequent transits, large atmospheric scale heights,

and favorable orbital geometry make them the most accessible exoplanets to characterize. These planets have been extensively observed with HST, Spitzer and ground-based telescopes (e.g., H. A. Knutson et al. 2007; D. K. Sing et al. 2016; D. Ehrenreich et al. 2020), and more recently with JWST (e.g., L. Alderson et al. 2023; A. D. Feinstein et al. 2023), with recent milestones including the detection of quartz clouds and photochem-

Corresponding author: Aaron Bello-Arufe  
[aaron.bello.arufe@jpl.nasa.gov](mailto:aaron.bello.arufe@jpl.nasa.gov)

ically produced SO<sub>2</sub> in their atmospheres (S.-M. Tsai et al. 2023; D. Grant et al. 2023).

By contrast, low-temperature ( $T_{\text{eq}} < 400$  K) transiting giants remain unexplored. A handful of these planets are known to transit their host stars, and some are highly suitable for atmospheric characterization via transmission spectroscopy. Many of these planets orbit G-type stars on long-period ( $\gtrsim 100$  days) orbits (e.g., L. Mancini et al. 2016; C. A. Beichman et al. 2018) and, unlike the vast majority of exoplanets probed with transit spectroscopy, they are not expected to be tidally locked (A. P. Showman et al. 2015). As a result, any longitudinal temperature gradients in their atmospheres should be orders of magnitude smaller than for hot Jupiters.

At temperatures intermediate between those of Jupiter/Saturn and those of hot Jupiters, we expect to see a unique atmospheric chemistry. At  $T_{\text{eq}} < 400$  K, CH<sub>4</sub> is the dominant carbon-bearing molecule, and a substantial fraction of nitrogen is expected to be in NH<sub>3</sub> (J. J. Fortney et al. 2020; K. Ohno & J. J. Fortney 2023), with many low-temperature giant exoplanets also remaining warm enough to avoid H<sub>2</sub>O condensation. This trait makes temperate gas giants ideal targets to measure the atmospheric abundances of C, N, and O and constrain their feeding zones and migration histories (e.g., K. I. Öberg et al. 2011; C. Mordasini et al. 2016; N. Espinoza et al. 2017; M. Ali-Dib 2017; A. J. Cridland et al. 2019, 2020). Moreover, photochemical processes that drive hydrocarbon formation in the Jovian atmosphere (G. R. Gladstone et al. 1996; J. Moses et al. 2005) instead result in the formation of HCN over hydrocarbons in warmer gas giants (R. Hu 2021), with quantitative predictions depending on  $K_{zz}$  and chemical networks (X. Yu et al. 2021; S.-M. Tsai et al. 2021a). The mechanisms to form HCN have been studied extensively for Titan (e.g., V. Vuitton et al. 2019), early Earth (e.g., V. Airapetian et al. 2016; P. B. Rimmer & S. Rugheimer 2019), and hot Jupiters (e.g., M. R. Line et al. 2011; Y. Kawashima & M. Ikoma 2018; R. Hobbs et al. 2019). Low-temperature giant exoplanets thus fill the temperature gap between Titan and hot Jupiters and can provide valuable empirical constraints on the formation of HCN on early Earth.

With a Transmission Spectroscopy Metric of 107, the newly confirmed planet TOI-199 b ( $0.810 \pm 0.005 R_J$ , M. J. Hobson et al. 2023) stands out as one of the most favorable low-temperature giant planets for atmospheric characterization. Its mass and radius suggest a Saturn-like internal structure with an H<sub>2</sub>-dominated atmosphere. The planet orbits its G9V host star every 105 days, receiving 2.5 times Earth's irradiation, which corresponds to a zero-albedo equilibrium temperature

of 352 K. Its relatively low mass ( $0.17 \pm 0.02 M_J$ ) and eccentricity ( $0.09^{+0.01}_{-0.02}$ ) suggest a low internal heat flux (below that of modern-day Jupiter) and further solidify TOI-199 b as a canonical test case for temperate giant exoplanets. Here we present the first atmospheric reconnaissance of TOI-199 b from a single transit observed with JWST/NIRSpec G395M.

## 2. OBSERVATIONS AND DATA REDUCTION

As part of JWST's General Observer program 5177 (P.I. Hu), we observed a transit of TOI-199 b on Dec 23, 2024 UTC. We collected the data using the Near InfraRed Spectrograph (NIRSpec, P. Jakobsen et al. 2022; S. M. Birkmann et al. 2022) with the medium-resolution grating G395M ( $R \sim 1000$ ), the SUB2048 subarray, and 7 groups per integration.

According to the JWST Exposure Time Calculator (ETC), the TOI-199 system ( $m_J = 9.3$ ) is bright enough to saturate the NIRSpec wide aperture target acquisition (WATA). We instead chose a nearby infrared source as the acquisition target. However, due to target acquisition failure, the nearby source fell outside the aperture during the observations, and instead the WATA found a noise peak of  $\sim 80$  counts in the centroiding box (at least  $\sim 150$  are typically required). As a result, our observations plausibly picked up the far wings of the point-spread function (PSF) of the science target or a diffraction spike. However, the differential nature of the transit measurement enabled us to still extract a useful transmission spectrum, with uncertainties  $\sim 4-5$  larger than predicted from PandExo (N. E. Batalha et al. 2017).

To ensure that our results are robust against different data treatment approaches, we performed two independent data reductions, which we detail below.

### 2.1. *Eureka!* reduction

We reduced the data using version 1.1 of the *Eureka!* pipeline (T. Bell et al. 2022). *Eureka!* is structured into six stages: the first two stages calibrate the raw data; stage 3 performs optimal extraction; stages 4 and 5 generate and fit the lightcurves, respectively; and stage 6 displays the results. Our *Eureka!* setup was informed by prior applications to other NIRSpec datasets (M. Damiano et al. 2024; A. Bello-Arufe et al. 2025; R. Hu et al. 2025), but with modifications to minimize the noise in the resulting lightcurves and including additional steps to mitigate the systematics introduced by the failed WATA, all of which are described below.

Starting from the uncalibrated raw data in the NRS1 detector (i.e. the `*nrs1_uncal.fits` files), we ran stages 1 and 2 of *Eureka!*. These stages call a series of steps from the `jwst` pipeline (version 1.15.1, H. Bushouse

et al. 2024) to perform initial processing and calibration. We ran all the default steps for NIRSpec time-series observations (TSO) data, except for the flat-field and photometric calibration steps. For the jump step, which identifies “up-the-ramp” outliers in each pixel, we increased the sigma threshold from the default value of 4 to a more conservative value of 7. To correct the superbias, we used the mean scale factor over all integrations. Prior to fitting the ramps, we performed group-level background subtraction using the average value in each detector column but excluding a region with a half-width of 8 pixels centered around the trace.

After calibration of the raw files, we ran *Eureka!*’s stage 3. Here, we extracted the detector columns 686–2044, which contain the spectral trace. We masked pixels with an odd data quality (DQ) entry, and we corrected the curvature of the trace by shifting each detector column by a whole number of pixels. To determine the position of the source, we fit a gaussian function to each detector column. We applied another round of column-by-column background subtraction, this time using the average value of pixels located at least 9 pixels away from the center of the trace, with a  $5\sigma$  threshold for outlier rejection. For the optimal extraction of the spectra, we used an aperture with a half-width of 3 pixels and constructed the spatial profile using the median frame after clipping  $5\sigma$  outliers and smoothing it with a window length of 13. We then masked three excessively noisy detector columns: 1488, 1661, and 1798.

In stage 4, we generated spectroscopic lightcurves from 2.87–5.17  $\mu\text{m}$ , with a bin size of  $\Delta\lambda = 0.004 \mu\text{m}$ , which closely matches the native spectral resolution of NIRSpec G395M ( $R \sim 1000$ ). However, in order to test the robustness of our results against different binning schemes, we produced a second set of lightcurves at  $\Delta\lambda = 0.025 \mu\text{m}$ . We cleaned each lightcurve using a rolling boxcar filter with a width of 10 data points that recursively clipped  $5\sigma$  outliers, up to 20 iterations.

The top panel in Figure 1 shows the raw spectroscopic lightcurves. While the transit of TOI-199 b is clearly visible around the middle of the observations, the lightcurves show wavelength-correlated noise. This systematic noise is caused by the failed WATA and, fortunately, is achromatic. As shown in Figure 1, we can effectively correct this noise by dividing out each spectroscopic lightcurve by a common-mode noise model.

To construct the common-mode noise model, we divided the white lightcurve by the best-fit model, which consisted of a `batman` transit model (L. Kreidberg 2015) multiplied by a systematics model (see e.g., F. Murgas et al. 2019; G. Fu et al. 2024). In our transit model, we fixed the period  $P$ , eccentricity  $e$ , and argument of

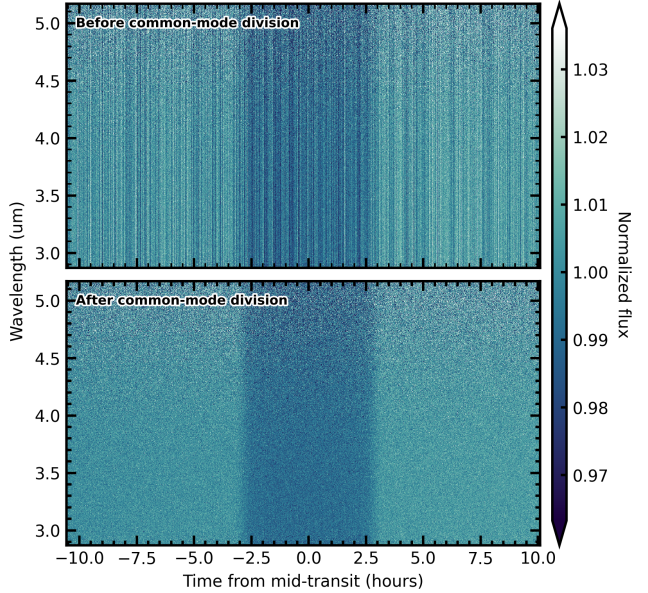


**Figure 1.** Raw spectroscopic lightcurves, as extracted with *Eureka!* and binned to  $\Delta\lambda = 0.004 \mu\text{m}$ , before and after dividing out the common-mode noise model.

periastron  $\omega$  to the values reported by M. J. Hobson et al. (2023), and we assigned uniform priors to the remaining transit and orbital parameters, namely the planet-to-star radius ratio  $R_p/R_\star$ , the transit time  $T_0$ , the orbital inclination  $i_p$ , and the scaled semimajor axis  $a/R_\star$ . We also fitted for the quadratic limb-darkening coefficients ( $q_1, q_2$ , D. M. Kipping 2013), to which we assigned uniform priors between 0 and 1. Meanwhile, the systematics model consisted of a linear polynomial in time, and we also included a white noise multiplier to boost the error bars to match the scatter of the residuals. We performed the white lightcurve fits using the dynamic nested sampling package `dynesty` (J. S. Speagle 2020), which is included in *Eureka!*’s stage 5. We used 2000 live points and set a convergence tolerance of  $\Delta \log Z < 0.001$ . The goal of this initial white lightcurve fit is solely to generate the common-mode noise model that is subsequently divided out from each spectroscopic lightcurve.

We then produced a second white lightcurve fit, which we used to report the system parameters and fix them in the spectroscopic lightcurve fits. One of the differences between this white lightcurve fit and the previous one is that our new systematics model additionally includes linear decorrelation against the  $x$  and  $y$  position and width of the trace. This choice is motivated by an improvement in the Bayesian evidence. Another difference is that we now also included a step function to account for the shift in the position of the trace happening around egress (see Figure 2), which results in

**Table 1.** Prior and Posterior System Parameter Distributions for **Eureka!**'s White Lightcurve Fit.

Parameter	Prior	Posterior
$T_0$ (BJD <sub>TDB</sub> –2 460 668)	$\mathcal{U}(0.15, 0.25)$	$0.21244^{+0.00039}_{-0.00039}$
$i_p$ ( $^\circ$ )	$\mathcal{U}(89.25, 90)$	$89.737^{+0.024}_{-0.021}$
$a/R_s$	$\mathcal{U}(50, 450)$	$119.1^{+3.0}_{-2.8}$
$P$ (days)	104.854 (fixed)	104.854 (fixed)
$e$	0.09 (fixed)	0.09 (fixed)
$\omega$	350 (fixed)	350 (fixed)
$R_p/R_s$	$\mathcal{U}(0.05, 0.15)$	$0.10268^{+0.00064}_{-0.00068}$
$q_1$	$\mathcal{U}(0, 1)$	$0.028^{+0.030}_{-0.016}$
$q_2$	$\mathcal{U}(0, 1)$	$0.29^{+0.39}_{-0.22}$

NOTE— $\mathcal{U}(a, b)$  is the uniform distribution between values  $a$  and  $b$ . The posterior values are reported as the median, with uncertainties given by the 16<sup>th</sup> and 84<sup>th</sup> percentiles.

a jump in the lightcurve flux. Indeed, we found that linear decorrelation alone was not sufficient to account for the full extent of the jump in flux, and Bayesian model comparison favors including a step function in the fits. We assigned a uniform prior to the step time and a normal prior centered around 0 to the step size. The third and final difference is binning of the lightcurve. The root mean square (RMS) of the residuals decreases more steeply than the  $N^{-1/2}$  scaling expected for uncorrelated noise, indicating the presence of high-frequency correlations (Figure 3, top panel). We binned the white lightcurve in time by a factor of 40 to mitigate these correlations, while still retaining sufficient points across the ingress and egress to accurately resolve the transit shape (Figure 3, middle panel). The prior and posterior system parameter distributions from this fit are presented in Table 1, and the best-fit model is shown in Figure 2.

To generate the transmission spectrum, we fitted the spectroscopic lightcurves in the same manner as the second white lightcurve fit, but with the following modifications. First, we kept  $T_0$ ,  $i_p$ , and  $a/R_s$  fixed to the values listed in Table 1 but still fitted for the quadratic limb darkening coefficients. No temporal binning was applied to the spectroscopic lightcurves, since the RMS of the residuals behaves as expected for pure white noise after removing the common-mode signal (Figure 3, bottom panel). For computational reasons, we decreased the number of live points to 1000 and the convergence tolerance to  $\Delta \log Z < 0.01$ . To assess the impact of limb-darkening assumptions, we produced an additional reduction at  $\Delta\lambda = 0.004 \mu\text{m}$  with quadratic limb-darkening coefficients fixed to the values from the ExoTiC-LD package (D. Grant & H. R. Wakeford 2022), based on 3D stellar models (Z. Magic et al. 2015) and

the stellar parameters from M. J. Hobson et al. (2023):  $T_{\text{eff}} = 5255 \text{ K}$ ,  $\log g = 4.582$ , and  $[\text{Fe}/\text{H}] = 0.22$ . In total, we produced three reductions with **Eureka!**:

- (a)  $\Delta\lambda = 0.004 \mu\text{m}$ , with free limb darkening (our fiducial reduction).
- (b)  $\Delta\lambda = 0.025 \mu\text{m}$ , with free limb darkening.
- (c)  $\Delta\lambda = 0.004 \mu\text{m}$ , with fixed limb darkening.

## 2.2. *Tswift* reduction

We performed an additional independent reduction of the NIRSpec dataset with the Transit swift routine (**Tswift**). The general steps are similar to those used in G. Fu et al. (2022). The default JWST pipeline is first used to process the `uncal.fits` files to produce the `darkcurrentstep.fits` files. Then the spectral trace is masked out, and the unilluminated regions are used to perform column-by-column 1/f and background subtraction at the group level. Next, we use the RampFitStep from the JWST pipeline to create the `rampfitstep.fits` files. Then, we cleaned the bad pixels and extracted the spectral trace. Due to the source being outside the slit, and we are capturing the flux of the PSF wings, the spectral trace is broadened compared to typical observations. We decided to use a large 30-pixel-wide aperture for the spectra extraction. Then each frame is summed in the vertical direction to create the white and spectroscopic lightcurves.

We also measured the spectral trace drift as a function of time and found a sudden small jump in the y direction around the 6340th integration, approximately 12.8 hours after the beginning of the observation. Due to the source being mostly outside the slit, this smaller drift in telescope pointing leads to significant wavelength-dependent slit-loss. To correct for this jump, we fitted a scaling factor for all points after the 6340th integration. So for the white lightcurve fit, we used **batman** (L. Kreidberg 2015) with 8 total free parameters, including a linear slope, constant,  $R_p$ ,  $a/R_s$ , inclination, mid-transit time, y-shift coefficient, and a scale factor for all points after 6340th integration. Then we fixed the best-fit white light  $a/R_s$ , inclination, and mid-transit time values for the spectroscopic lightcurve fits while fitting for the remaining 5 parameters. The limb darkening parameters are fixed to the 3D Stagger-grid stellar models (Z. Magic et al. 2015). To check the robustness of fitting a scaling factor for all points after the 6340th integration, we also fit for the lightcurves with trimming all points after the 6340th integration. The resulting transit spectra from the two methods generally agree with a consistent shape. However, the trimming method results in larger error bars compared to the scaling factor approach due to the lack of egress and the subsequent

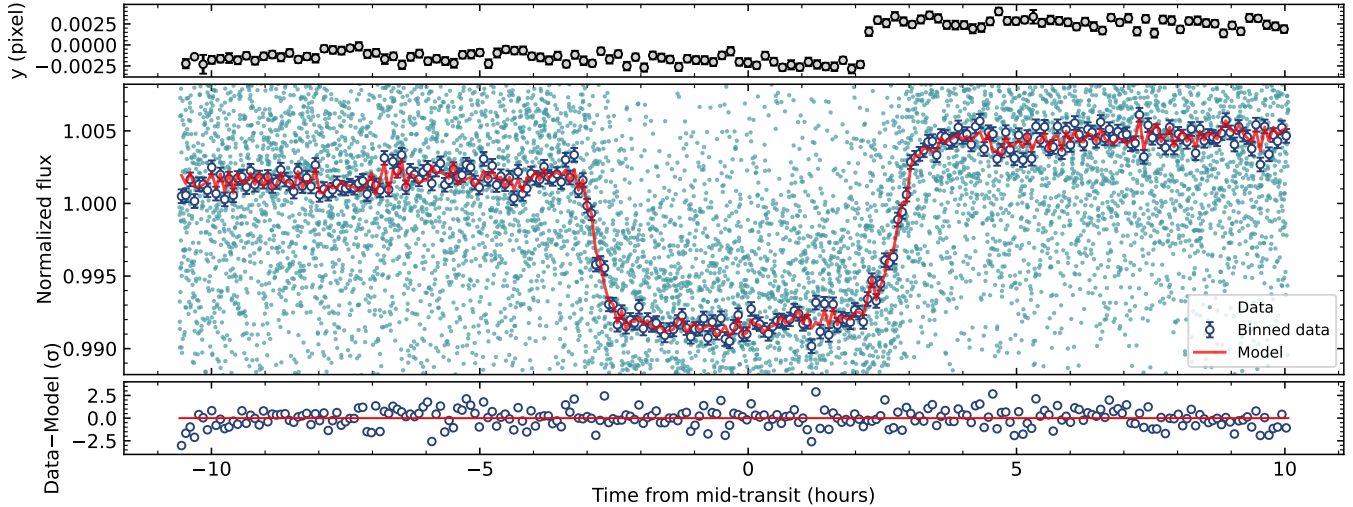


**Figure 2.** *Top:* Mean-subtracted position of the trace along the  $y$  (i.e. cross-dispersion) direction, binned by a factor of 80 to more easily visualize the jump occurring around egress. *Middle:* Raw and binned ( $\times 40$ ) white lightcurves of TOI-199 b’s transit, observed with NIRSpec G395M, including the best-fit model, as extracted with `Eureka!`. *Bottom:* Residuals from the best-fit model, measured in  $\sigma$ .

baseline. The transit spectra from both methods are consistent with the one from `Eureka!`. In Figure 4, we compare the transmission spectra from the two independent reductions. Apart from a small vertical offset, the spectra show overall agreement.

### 3. ATMOSPHERIC RETRIEVALS

To interpret the different reductions of the transmission spectra, we performed Bayesian atmospheric retrievals. To assess the robustness of our results, we applied two independent codes: `ExoTR` (M. Damiano et al. 2024, Tokadjian et al. 2025, in prep) and Aurora (L. Welbanks & N. Madhusudhan 2021).

#### 3.1. *ExoTR*

`ExoTR`<sup>12</sup> is an atmospheric forward model and retrieval framework, which uses a nested sampling algorithm via `MultiNest` (F. Feroz et al. 2009) and `PyMultiNest` (J. Buchner et al. 2014) to statistically interpret exoplanet transmission spectra. `ExoTR` maps molecular mixing ratios to their observable signatures, and it includes the ability to model realistic water clouds, hazes, and stellar activity (M. Damiano et al. 2024, Tokadjian et al. 2025, in prep). The framework has been applied across diverse targets—LHS-1140 b (cold, water-rich), L 98-59 b (potentially volcanic), Kepler-51 d (a hazy super-puff), and K2-18 b (temperate sub-Neptune)—to infer atmospheric conditions from transmission data (M. Damiano et al. 2024; A. Bello-Arufe et al. 2025; J. E. Libby-Roberts et al. 2025; R. Hu et al. 2025).

<sup>12</sup> <https://github.com/MDamiano/ExoTR>

We applied `ExoTR` to interpret the spectrum of TOI-199 b, fitting for a selected list of molecules and cloud parameters with uniform priors (Table 2), and with H<sub>2</sub> as the fill gas. The selection of these molecules was guided by insights from self-consistent atmospheric models (e.g., R. Hu 2021, and models developed in this work). The molecular opacities were calculated line-by-line using the most up to date line lists from HITEMP (R. J. Hargreaves et al. 2020) (CH<sub>4</sub>), ExoMol (J. Tennyson et al. 2016) (SO<sub>2</sub>), and HITRAN (I. E. Gordon et al. 2022) (all other molecules). Fixed parameters include the planet mass  $M_p = 54.04 M_\oplus$  and stellar properties (e.g., photospheric temperature of  $T_s = 5255\text{K}$ ) (M. J. Hobson et al. 2023).

Figure 5 shows the best-fit model and molecular contributions from the retrieval. Many features are dominated by CH<sub>4</sub>, especially in the 3.2–3.7  $\mu\text{m}$  range; indeed, we are able to constrain CH<sub>4</sub> abundance to  $\sim 1$  dex and obtain a Bayes factor of 790, suggestive of a significant preference in favor of a model including CH<sub>4</sub> relative to a CH<sub>4</sub>-free model. Other features are weakly fit with HCN, OCS, and/or CO<sub>2</sub> but these molecules, along with H<sub>2</sub>O, NH<sub>3</sub>, CO, SO<sub>2</sub>, and H<sub>2</sub>S, remain unconstrained. The 1D histogram for HCN suggests a hint of its presence, but the wide tail towards low abundance weakens any claim of robustness. Table 2 highlights the  $1\sigma$  confidence interval of the constrained species (CH<sub>4</sub>) and the  $2\sigma$  upper bounds for the unconstrained molecules.

We repeated the retrieval for three additional cases: the native spectral resolution data with fixed limb-darkening coefficients, data binned down to a resolution

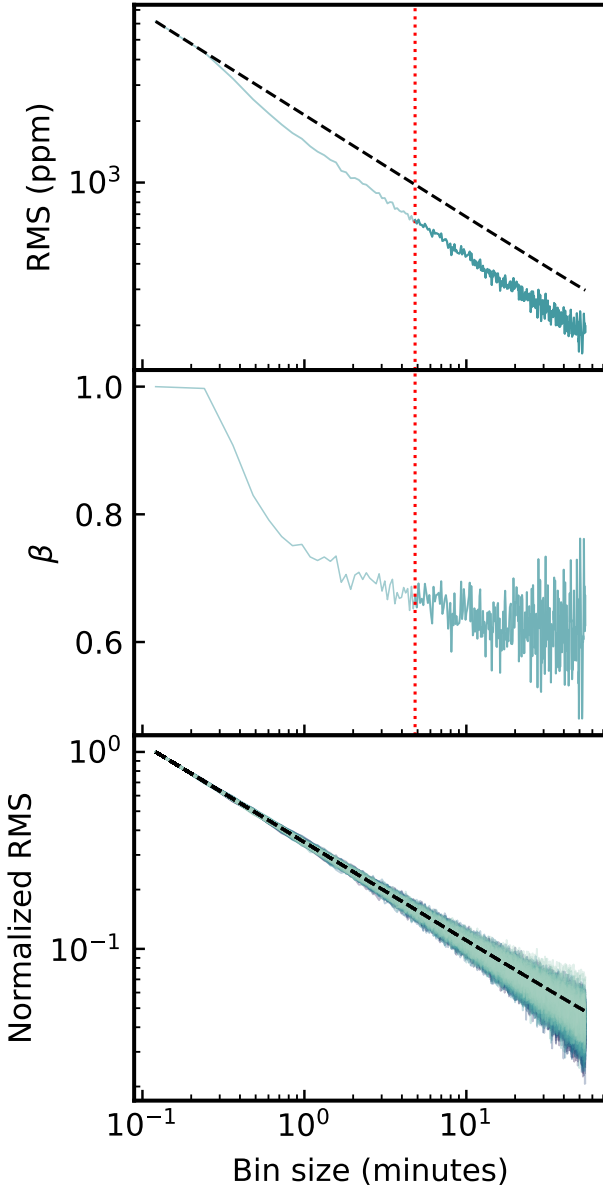


**Figure 3.** *Top:* RMS of the white lightcurve residuals as a function of bin size (solid teal line) and scaling expected for purely white noise (dashed black line). The dotted red line indicates the bin size used in the **Eureka!** white lightcurve fit (i.e. 40×). *Middle:* Ratio of the two lines in the top plot (i.e. red noise factor, J. N. Winn et al. 2008). *Bottom:* Normalized RMS of the residuals of the spectroscopic lightcurves from **Eureka!** as a function of bin size (solid colored lines) and scaling expected for purely white noise (dashed black line).

of 0.025 μm, and the data resulting from the **Tswift** reduction. Slight differences arise in the posterior solutions, but the main conclusions remain the same (see Figure 6).

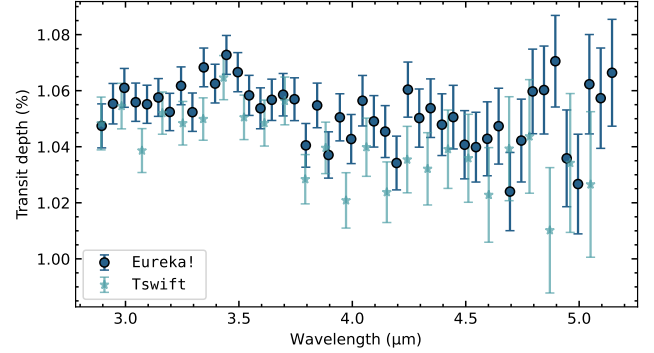


**Figure 4.** Comparison of the two independent reductions of the NIRSpec data of TOI-199 b.

**Table 2.** Prior and Posterior Parameter Distributions for the **ExoTR** fit to the reference **Eureka!** reduction.

Parameter	Prior	Posterior
Planetary radius [ $R_p(^1)$ ]	$\mathcal{U}(0.5, 2)$	$0.97^{+0.01}_{-0.02}$
Planetary temperature [K]	$\mathcal{U}(100, 500)$	$325^{+88}_{-82}$
Cloud top [Pa]	$\mathcal{LU}(-1.0, 6.0)$	$2.3^{+1.4}_{-1.0}$
VMR H <sub>2</sub> O	$\mathcal{LU}(-12, -0.3)$	< -2.05
VMR CH <sub>4</sub>	$\mathcal{LU}(-12, -0.3)$	$-2.46^{+0.85}_{-1.15}$
VMR NH <sub>3</sub>	$\mathcal{LU}(-12, -0.3)$	< -1.78
VMR HCN	$\mathcal{LU}(-12, -0.3)$	< -1.94
VMR CO	$\mathcal{LU}(-12, -0.3)$	< -3.55
VMR CO <sub>2</sub>	$\mathcal{LU}(-12, -0.3)$	< -3.47
VMR SO <sub>2</sub>	$\mathcal{LU}(-12, -0.3)$	< -4.85
VMR OCS	$\mathcal{LU}(-12, -0.3)$	< -3.12

NOTE— $\mathcal{LU}(a, b)$  is the log-uniform (Jeffreys) distribution between values  $a$  and  $b$ . Posteriors: Median values with  $1\sigma$  uncertainties. In the case of gases for which we did not obtain a detection, we present the upper limits corresponding to 95% ( $2\sigma$ ) cumulative probability levels.

NOTE - (<sup>1</sup>) M. J. Hobson et al. (2023).

We explored the effect of aerosols by repeating the baseline retrieval without the gray cloud, considering both a cloud-free atmosphere and scenarios with a Mie-scattering haze, using optical properties of tholin (i.e. Titan haze analog, B. N. Khare et al. 1984), soot (i.e. absorbing black carbon, M. Hess et al. 1998), and organic haze (i.e. water-rich tholin at 400 K C. He et al. 2024) individually to assess both the type and properties of hazes constrained by the data. We found no significant preference between a cloudy and cloud-free model, with a Bayes factor of only 2.29 for clouds. The Bayes factors for hazy atmosphere models with tholin, soot, or organics are similarly small, suggesting ambiguity in the data for the presence of haze (Table 3). However,

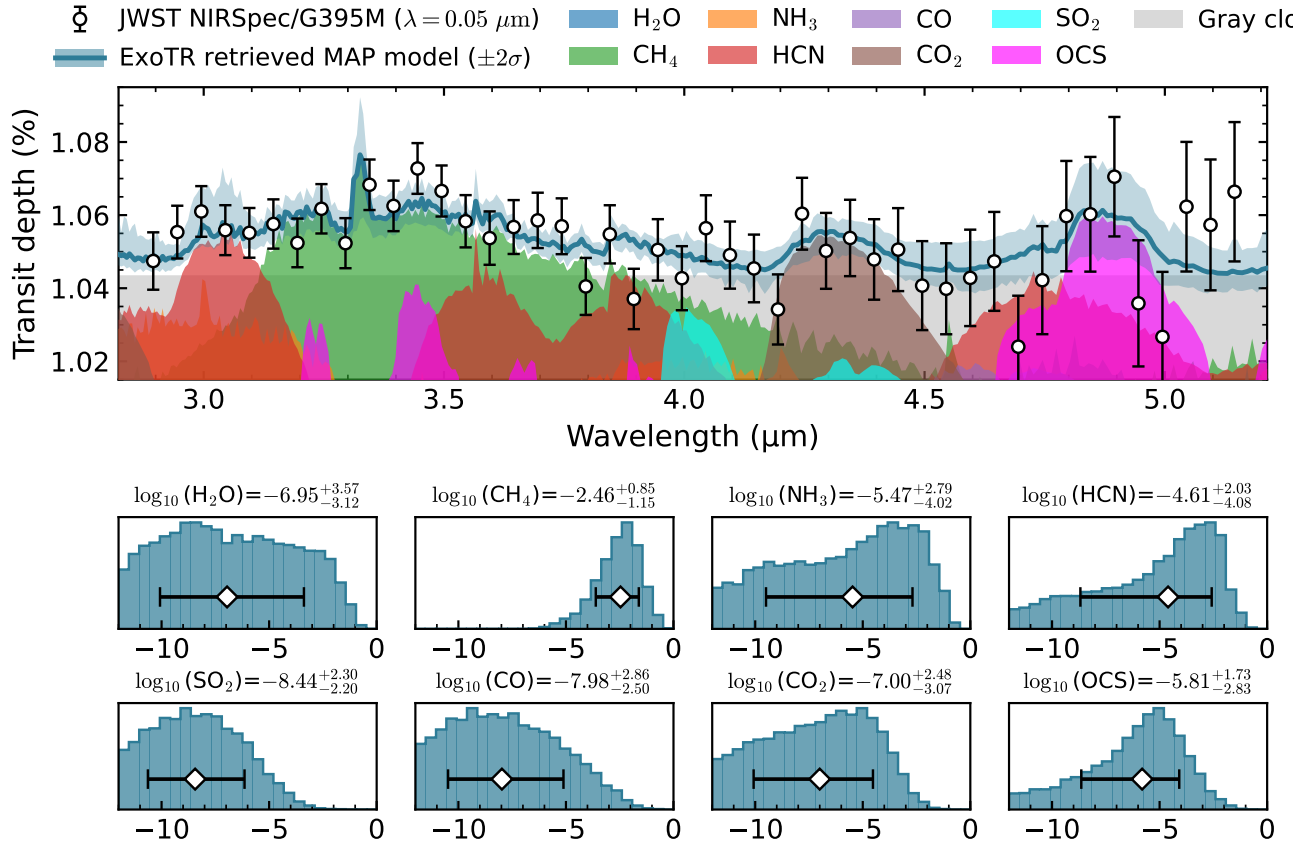


**Figure 5.** Top: Maximum A Posteriori (MAP) model and  $2\sigma$  credible regions from ExoTR retrievals on the fiducial reduction, overlaid with data binned at  $\Delta\lambda = 0.05 \mu\text{m}$ . Also shown are the contributions from each molecule and clouds to the transmission spectrum. Bottom: 1D histograms of the posterior distributions from the retrieval results, including the median and  $\pm 1\sigma$  uncertainties (i.e. 16<sup>th</sup> and 84<sup>th</sup> percentiles).

given the relationship between the atmospheric CH<sub>4</sub> and haze production, particularly for tholin and organics, we also test whether the evidence for haze increases for a CH<sub>4</sub>-free model. Indeed, we find that the Bayes factor does not change for soot, which is simple carbon, but does increase significantly for tholin and organics (up to 35 and 36, respectively, or “very strong” evidence according to D. P. Thorngren et al. 2025). Thus, the evidence for CH<sub>4</sub> in a hazy atmosphere correspondingly decreases, from 291 to 22 and 16 for tholin and organics, respectively (and up slightly to 471 for soot). The haze particle diameters in these models are quite small (median of  $0.015 \mu\text{m}$ ) and the abundances are quite high (median of 40 ppm), suggesting that an unusually large cross section for haze is needed to make up for the lack of CH<sub>4</sub>. Also, when comparing model evidence for CH<sub>4</sub> vs tholin/organic haze in analogous cases, there is always a preference for the CH<sub>4</sub> model by a factor of  $\sim 8$ . Since the presence of CH<sub>4</sub> is directly related to tholin and organic hazes, whether one model is preferred over the other does not change our main

conclusion that there is strong evidence for CH<sub>4</sub> in the atmosphere of TOI-199 b. We also note that the mixing ratio of CH<sub>4</sub> remains nearly constant across all haze and gray cloud models, with a maximum difference in the median abundances of  $\Delta \log(\text{CH}_4) = 0.28$ , well below the  $1\sigma$  uncertainties. To more rigorously constrain the presence or absence of clouds and hazes, additional transit data, especially at shorter wavelengths where a haze slope would be more prominent, would be especially helpful and would help to distinguish between a cloudy, clear, and hazy atmosphere.

### 3.2. Aurora

Aurora (L. Welbanks & N. Madhusudhan 2021) is a Bayesian retrieval and forward-modeling framework for interpreting exoplanet transmission and emission spectra (e.g., T. J. Bell et al. 2023; L. Welbanks et al. 2024). It solves the radiative transfer equation in a plane-parallel geometry under hydrostatic equilibrium, with flexible parameterizations of the atmospheric temperature structure, composition, and cloud/haze properties.

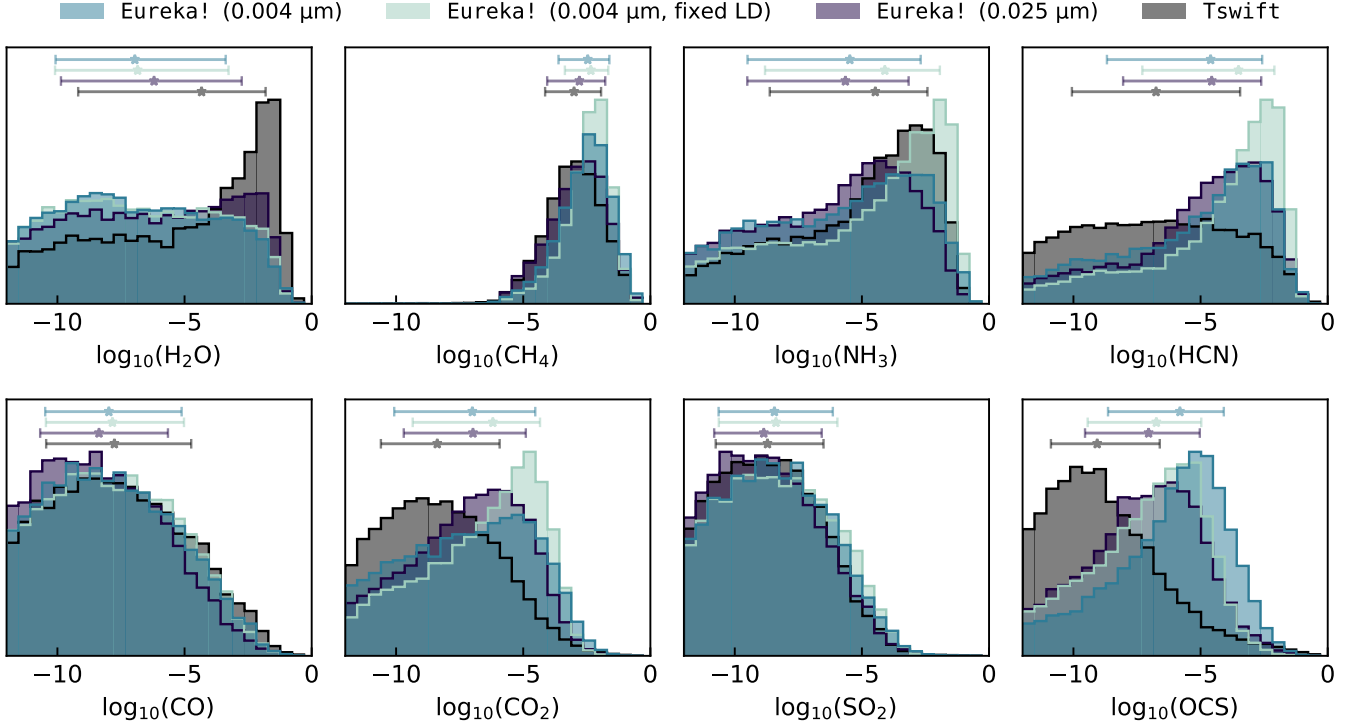


**Figure 6.** Posterior distributions of the gas abundances from the ExoTR retrievals on the different data reductions. Medians and  $1\sigma$  uncertainties are overplotted as markers with horizontal error bars.

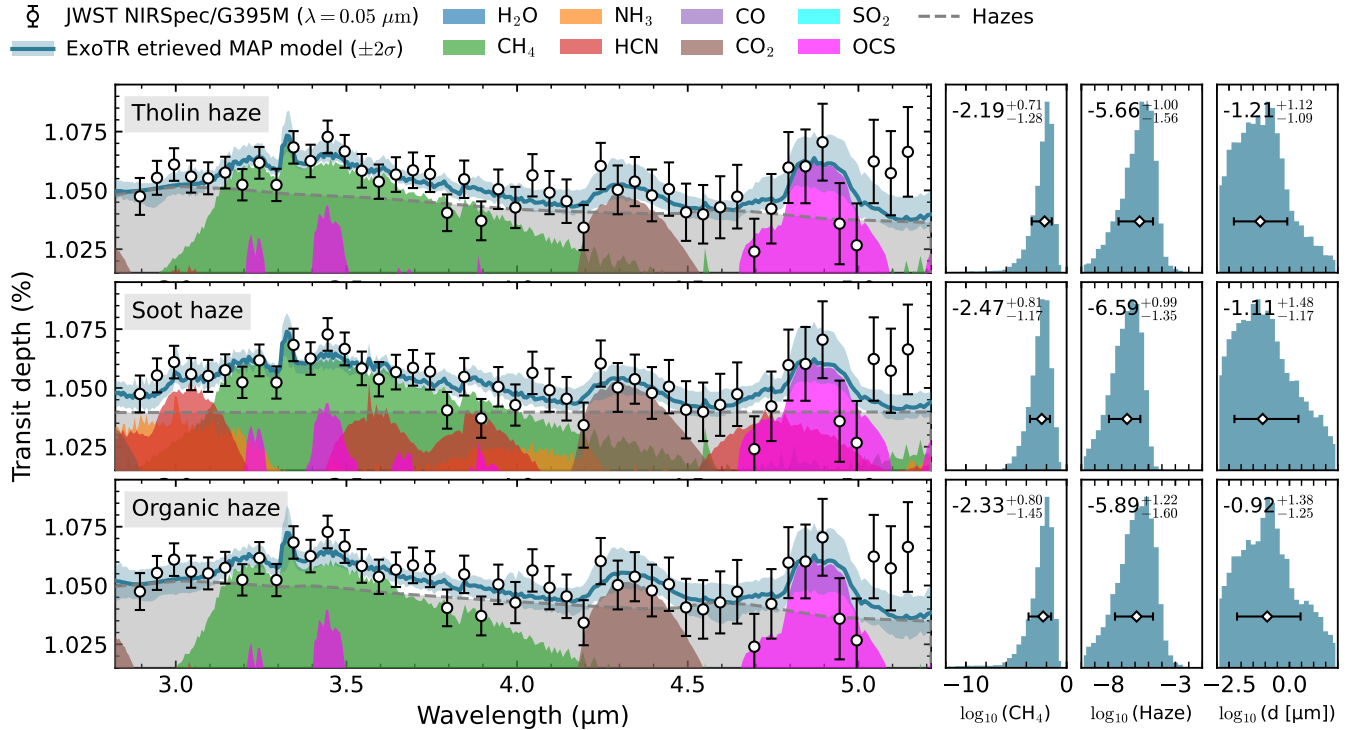


**Figure 7.** Same as Figure 5, but for models that include a tholin haze (top), a soot haze (middle), and an organic haze (bottom). Next to each spectrum we show the corresponding 1D histograms of methane and the haze abundance and particle diameter.

**Table 3.** Bayes factor (BF) for CH<sub>4</sub> and various haze types from ExoTR retrievals.

Baseline Case	BF(CH <sub>4</sub> )	BF(Haze)	Ratio
clear, no CH <sub>4</sub>	291	35 (tholin)	8.3
		36 (organics)	8.1
		1.6 (soot)	180
tholin w/ CH <sub>4</sub>	22.4	2.68	8.4
organics w/ CH <sub>4</sub>	16.1	2.00	8.1
soot w/ CH <sub>4</sub>	47.1	2.61	180

NOTE—For the first block, the baseline is a clear atmosphere with no CH<sub>4</sub>. We report the Bayes factor for adding CH<sub>4</sub> vs. adding each haze type individually. For the remaining 3 rows, the baseline contains both haze and CH<sub>4</sub>, and we assess the Bayes factor by removing either the CH<sub>4</sub> or the haze, one at a time.

Using this complementary framework, we tested the dependence of the retrieved atmospheric properties on the specific model assumptions considered in the main analysis from ExoTR in Section 3.1. This approach allows us to assess how model degeneracies (e.g., L. Welbanks & N. Madhusudhan 2019, 2022) and model construction choices (e.g., L. Welbanks et al. 2025) affect the interpretation of the atmospheric spectrum. Parameter estimation was performed using MultiNest (F. Feroz et al. 2009) via PyMultiNest (J. Buchner et al. 2014).

We explored three sets of modifications relative to the ExoTR baseline model to evaluate the robustness of retrieved CH<sub>4</sub>, NH<sub>3</sub>, and HCN abundances. Specifically, we considered 1) the relaxation of the isothermal temperature assumption, and 2) incorporating inhomogeneous cloud and haze cover. We performed retrievals using the model configurations described below on all reductions.

These atmospheric models considered the same absorbers as ExoTR (e.g., H<sub>2</sub>O (L. S. Rothman et al. 2010), CH<sub>4</sub> (S. N. Yurchenko & J. Tennyson 2014), NH<sub>3</sub> (S. N. Yurchenko et al. 2011), HCN (R. J. Barber et al. 2014), CO (L. S. Rothman et al. 2010), CO<sub>2</sub> (L. S. Rothman et al. 2010), SO<sub>2</sub> (D. S. Underwood et al. 2016), OCS (J. S. Wilzewski et al. 2016)). The opacities were computed line-by-line from the HITRAN (L. S. Rothman et al. 2010; C. Richard et al. 2012), HITEMP (R. J. Hargreaves et al. 2020), and ExoMol (J. Tennyson et al. 2016) databases, following the prescriptions in L. Welbanks & N. Madhusudhan (2021); L. Welbanks et al. (2024).

Aurora accounts for the effects of inhomogeneous clouds and hazes modeled as a linear combination of a clear and cloudy/hazy region, following the cloud deck prescription and enhanced H<sub>2</sub>-Rayleigh scattering

described in L. Welbanks & N. Madhusudhan (2021), which builds upon the works of A. Lecavelier Des Etangs et al. (2008); M. R. Line & V. Parmentier (2016); R. J. MacDonald & N. Madhusudhan (2017). For the non-isothermal temperature structure, we adopted the 6 parameter prescription from N. Madhusudhan & S. Seager (2009). All model spectra were computed at a resolving power of  $R = 50,000$  over the wavelength range of 2.5 to 5.5  $\mu\text{m}$ .

The retrieved spectra and posteriors from the analysis on the Eureka! reduction with  $\Delta\lambda = 0.004 \mu\text{m}$  are shown in Figure 8. For visual clarity, the shown data are binned. The retrieved atmospheric temperature structure is non-isothermal with  $T=494^{+283}_{-157} \text{ K}$  at 100 mbar, which is consistent with the planet’s equilibrium temperature. The retrieved abundances of NH<sub>3</sub>, H<sub>2</sub>O, CO, CO<sub>2</sub>, HCN, and OCS remain poorly constrained as with the analysis from ExoTR. However, the spectrum near  $\sim 3 \mu\text{m}$  seems to be preferentially explained by the rovibrational absorption line of NH<sub>3</sub> rather than clouds as with the ExoTR analysis. Model comparison between the model including the species and the model excluding it suggests no meaningful preference for the inclusion of NH<sub>3</sub>.

Nonetheless, the interpretation of the spectrum of TOI-199 b as being largely explained by the methane feature at  $\sim 3.3 \mu\text{m}$  and its broadband feature remains consistent. The retrieved CH<sub>4</sub> abundance is comparable with that derived from ExoTR although generally higher. This is consistent with expectations from known degeneracies between molecular abundances and the presence of inhomogeneous clouds/hazes (e.g., L. Welbanks & N. Madhusudhan 2019, 2021; M. C. Nixon et al. 2024). The preference for the model including CH<sub>4</sub> over the model without the absorber is marginally lower, with a Bayes factor of 705. The preference for the full over a model without NH<sub>3</sub> or without NH<sub>3</sub> and HCN is weak, with Bayes factors of 2. We emphasize that this model preference is relative to the specific set of molecules considered. Furthermore, including more species such as C<sub>2</sub>H<sub>6</sub>, C<sub>2</sub>H<sub>2</sub>, C<sub>2</sub>H<sub>4</sub>, or other molecules considered in the full forward models (presented in Section 4), could alter the outcome (L. Welbanks et al. 2025).

## 4. SELF-CONSISTENT MODELS

### 4.1. Forward model setup

We modeled the atmosphere of TOI-199 b using the climate module of EPACRIS (described in R. Hu et al. (2024) and also applied in M. Damiano et al. (2024); J. Yang & R. Hu (2024a); A. Bello-Arufe et al. (2025)). EPACRIS-Climate solves for the 1-D radiative-convective equilibrium using the improved 1-D two-

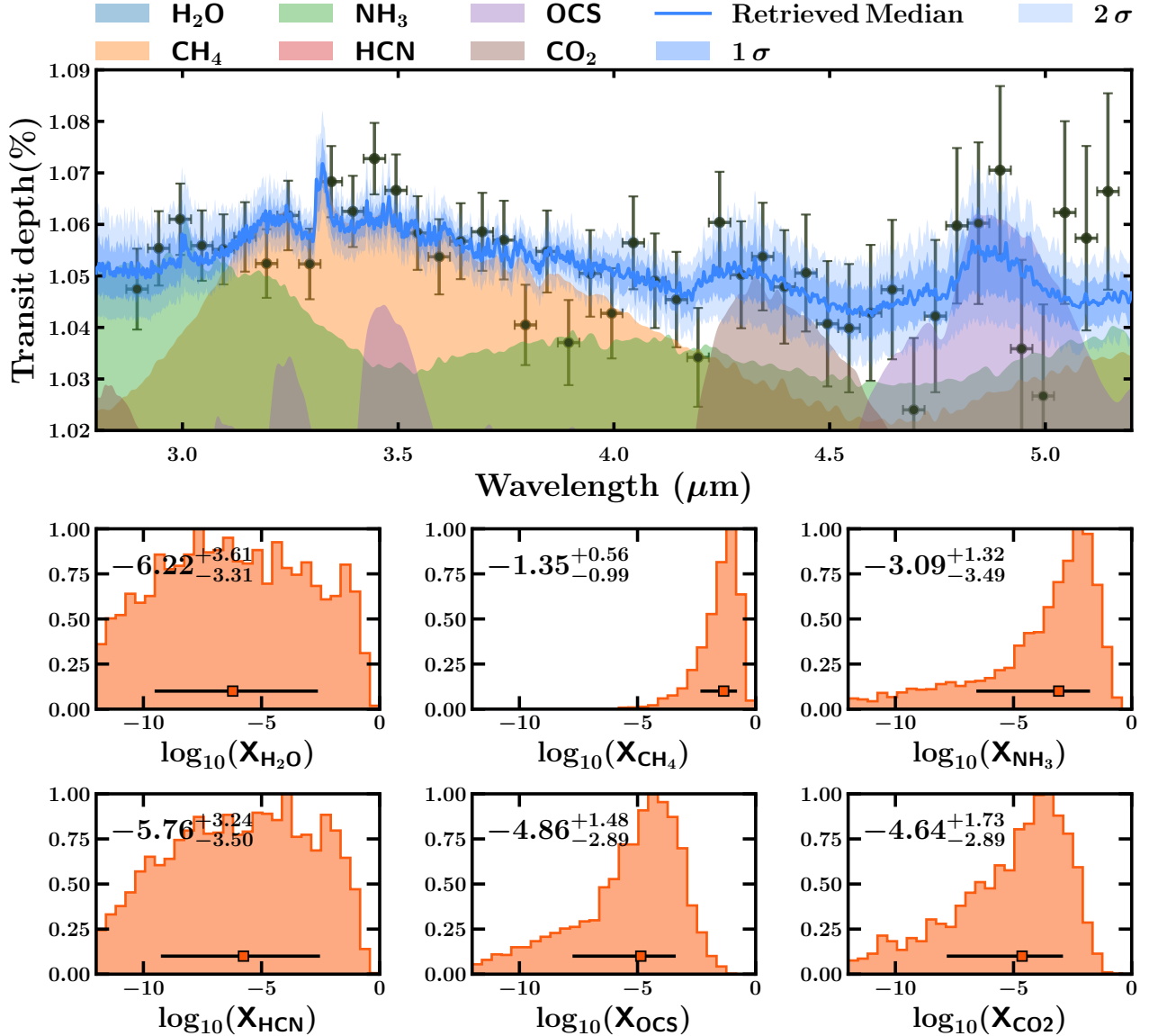


**Figure 8.** Top: Best-fit spectrum with  $1\sigma$  and  $2\sigma$  model posteriors, from retrievals using Aurora and molecule contributions from the best fit model. Bottom: Posterior distributions for the molecules of interest, including the median and  $\pm 1\sigma$  uncertainties.

stream radiative solver (K. Heng et al. 2018). The temperature-pressure (TP) profiles were computed assuming chemical equilibrium abundances for solar and enhanced metallicity cases ( $\text{M/H} = 10$ , corresponding to 10 times solar metallicity), as well as for solar and super-solar C/O ratios (0.59 and 1.1). However, we found that the C/O ratio has little effect on the resulting atmospheric characteristics. The solar elemental abundances were taken from M. Asplund et al. (2021). We assumed full heat redistribution ( $f=0.25$ ), a null Bond albedo, and a nominal internal temperature of  $T_{\text{int}} = 50 \text{ K}$ . Gas giants exhibit a wide range of possible internal temperatures, which depend on their mass, age, evolution history, and orbital eccentricity (J. J. Fortney et al. 2020).

Thus, we also examined cases with increased internal temperatures up to 200 K. To calculate the lapse rate, we employed the multi-component pseudo-adiabat equation derived by R. J. Graham et al. (2021). For the opacities, we used all major expected species:  $\text{H}_2\text{O}$ ,  $\text{NH}_3$ ,  $\text{CH}_4$ ,  $\text{SO}_2$ ,  $\text{CO}_2$ ,  $\text{CO}$ ,  $\text{H}_2\text{S}$ ,  $\text{NO}_2$ ,  $\text{NO}$ ,  $\text{N}_2$ ,  $\text{O}_2$ ,  $\text{OH}$ ,  $\text{HO}_2$ ,  $\text{HCN}$ , OCS,  $\text{O}_3$ ,  $\text{C}_2\text{H}_6$ ,  $\text{CH}_2\text{O}_2$ ,  $\text{HNO}_3$ ,  $\text{N}_2\text{O}$ ,  $\text{C}_2\text{H}_2$ ,  $\text{C}_2\text{H}_4$ ,  $\text{H}_2\text{CO}$ , and  $\text{H}_2\text{O}_2$ , as well as collision-induced absorbers  $\text{H}_2-\text{H}_2$ ,  $\text{H}_2-\text{He}$ ,  $\text{H}_2-\text{H}$ ,  $\text{H}_2-\text{N}_2$ ,  $\text{N}_2-\text{N}_2$ , and  $\text{CO}_2-\text{CO}_2$ . The sources for the different opacities are the same as those listed in Section 3.1. For all forward models, we used the PHOENIX (T. O. Husser et al. 2013) stellar spectrum.

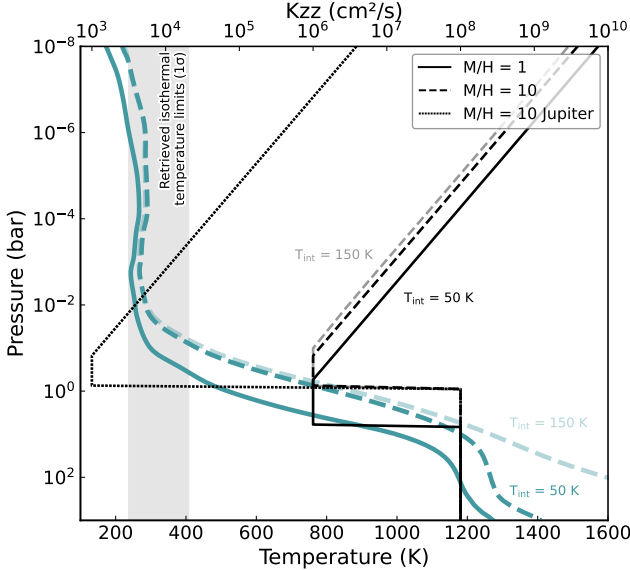


**Figure 9.** Temperature-pressure (TP) and eddy diffusion profiles ( $K_{zz}$ ) for TOI-199 b. TP profiles (teal curves) are computed assuming equilibrium chemistry.  $K_{zz}$  profiles (black curves) are derived from the respective TP profiles. Solid curves represent solar metallicity cases ( $M/H = 1$ ), whereas dashed curves are for enhanced metallicity ( $M/H = 10$ ). Faint curves represent the case with increased internal temperature. The dotted  $K_{zz}$  profile represents a Jupiter-like mixing case. The gray region indicates the retrieved  $1\sigma$  temperature limits obtained from ExoTR spectral retrievals.

The profiles were converged to full radiative-convective equilibrium, accounting for potential condensates. The resulting TP profiles for  $C/O = 0.59$  are shown in Fig. 9. The solid curves represent models with  $T_{int} = 50$  K, while the faint curves correspond to a case with increased internal heating ( $T_{int} = 150$  K). TP profiles for  $C/O = 1.1$  did not show substantial differences and are therefore not shown.

1D photochemical kinetic-transport atmospheric modeling also requires an eddy diffusion coefficient profile ( $K_{zz}$ ), which we derived from the converged TP profiles for both solar and enhanced metallicity cases. We assumed  $K_{zz}$  to be constant in the convective region ( $K_{zz} = 10^6 \text{ cm}^2 \text{s}^{-1}$ ) and the deep atmosphere ( $K_{zz} = 10^8 \text{ cm}^2 \text{s}^{-1}$ ). The convective region value of  $10^6 \text{ cm}^2 \text{s}^{-1}$  was estimated to be comparable to planets with a similar  $T_{eq}$  based on X. Zhang & A. P. Showman (2018). The deep atmosphere value of  $10^8 \text{ cm}^2 \text{s}^{-1}$  was originally derived from GeH<sub>4</sub> observations in Jupiter (G. L. Bjoraker et al. 2018) and has been commonly adopted to describe Jupiter's deep atmospheric vertical mixing (D. Wang et al. 2016). However, recent work suggests that Jupiter's deep interior  $K_{zz}$  should be lower than this

value according to 1D-2D coupled approaches (J. Yang et al. 2025), requiring caution when adopting deep interior  $K_{zz}$  values. For comparison, we also ran models with a Jupiter-like  $K_{zz}$  profile with  $K_{zz} = 10^3 \text{ cm}^2 \text{s}^{-1}$  in the convective region, as well as a set of cases with uniform  $K_{zz}$  values ranging from  $10^4$  to  $10^8 \text{ cm}^2 \text{s}^{-1}$ . Above the convective region,  $K_{zz}$  was assumed to increase with the inverse square root of pressure (R. S. Lindzen 1981) as described in Equation 28 of S.-M. Tsai et al. (2021b). The adopted  $K_{zz}$  profiles are presented in Fig. 9.

Using the TP and  $K_{zz}$  profiles described above, we ran a suite of photochemical simulations with the chemistry module of EPACRIS (J. Yang & R. Hu 2024a), adopting the chemical network of J. Yang & R. Hu (2024b); R. Hu et al. (2025); J. Yang (2025) (99 species and 2024 reactions in total) and the same PHOENIX stellar spectrum as described previously. We note that PHOENIX models typically underestimate UV flux (P. R. Behr et al. 2023), which may lead to slightly conservative estimates of photodissociation rates affecting photochemically produced species.

To generate the corresponding transmission spectra, we used the radiative-transfer code petitRADTRANS<sup>13</sup> (P. Mollière et al. 2019, 2020). Spectra were computed at a resolving power of  $\lambda/\Delta\lambda = 1000$ ; although the figures display binned versions for clarity, the full-resolution spectra were used to compute  $\chi^2$  values for all forward models. For the reference pressure defining the radius of the planet we used  $P_0 = 1$  bar. Most molecular opacities in petitRADTRANS were taken from the ExoMol database<sup>14</sup> (K. L. Chubb et al. 2021). A complete list of opacities and their line-list sources is provided in Table A.1 of M. Zilinskas et al. (2025).

#### 4.2. Disequilibrium chemistry results

In Figure 10 we show the major photochemical abundances for an atmosphere with enhanced solar metallicity ( $M/H = 10$ ) and the nominal  $K_{zz}$  profile. At  $M/H = 10$  and  $T_{int} = 50$  K (solid curves), the dominant carbon carrier is predicted to be CH<sub>4</sub>, which is closely followed by CO. NH<sub>3</sub> is the dominant nitrogen species in the probed region, with an average volume mixing ratio (VMR) of  $10^{-3}$  that exceeds HCN by approximately two orders of magnitude. TOI-199 b's irradiation is high enough to dissociate most H<sub>2</sub>S molecules, resulting in ample atomic sulfur and HS radicals. This allows for efficient formation of CH<sub>3</sub>SH and OCS. CH<sub>3</sub>SH forms through the H<sub>2</sub>S and HS interaction with the CH<sub>3</sub> radi-

<sup>13</sup> <http://gitlab.com/mauricemolli/petitRADTRANS>; version 2 was used for this work

<sup>14</sup> <https://www.exomol.com/>

cal, making it the primary sulfur molecule (R. Hu et al. 2025). Temperate conditions also make OCS more abundant than  $\text{SO}_2$ , with the latter being more dominant in hot Jupiters (S.-M. Tsai et al. 2023; J. Yang & R. Hu 2024b).

At zero Bond albedo, none of the major species are predicted to condense out in the atmosphere of TOI-199 b, allowing  $\text{H}_2\text{O}$  to retain its dominance. However, as discussed later, its contribution to the transmission spectrum within the NIRSpec wavelength range is relatively small, leading to an unconstrained abundance measurement.

The shift to a higher internal temperature has important implications for the resulting composition (dashed curves, Fig. 10). While the main carbon and oxygen carriers remain  $\text{CH}_4$  and  $\text{H}_2\text{O}$ , respectively, CO abundance is increased substantially, nearly overtaking  $\text{CH}_4$ . Higher temperatures in the deep atmosphere also thermally disfavor  $\text{NH}_3$ , decreasing its VMR by approximately an order of magnitude. At pressures larger than 100 bar, this allows for HCN to increase drastically; however, due to its dependence on  $\text{NH}_3$  for nitrogen supply, its VMR at probed atmospheric layers decreases with increasing  $T_{\text{int}}$ . We find that even at  $T_{\text{int}} = 100$  K,  $\text{NH}_3$  transmission features are heavily diminished and largely overtaken by the  $\text{H}_2\text{O}$  continuum. Other spectroscopically important species, such as  $\text{CO}_2$  or OCS, show relatively small abundance increases, resulting in slightly larger features between 4.2 – 5.1  $\mu\text{m}$ .

While not shown, we find that increasing the C/O ratio for a relatively low metallicity atmosphere results in only minor compositional changes. At C/O = 1.1,  $\text{CH}_4$  replaces  $\text{H}_2\text{O}$  as the dominant infrared opacity source, while other major oxygen carriers ( $\text{CO}$ ,  $\text{CO}_2$ , OCS) become slightly less abundant. Despite these changes, the transmission spectrum is only weakly affected, with the transit radius increasing for  $\text{CH}_4$  bands and decreasing at larger wavelengths where other major oxygen carriers dominate.

Fig. 10 also shows the  $1\sigma$  retrieved abundance of  $\text{CH}_4$  and  $2\sigma$  upper limits for all other major species (indicated by triangles). The arrow lengths represent  $1\sigma$  uncertainty ranges. For an enhanced metallicity atmosphere ( $\text{M}/\text{H} = 10$ ), the predicted  $\text{CH}_4$  abundance agrees well with the retrieved value, and all other major species besides CO fall within their respective constraints. However, as we discuss below, a solar-metallicity atmosphere is also consistent with the observed abundance limits.

Figure 11 compares a solar metallicity atmosphere (solid curves) to an enhanced metallicity case ( $\text{M}/\text{H} = 10$ ; dashed curves). The main atmospheric components –  $\text{CH}_4$ ,  $\text{NH}_3$ , and  $\text{H}_2\text{O}$  – scale nearly linearly with metal-

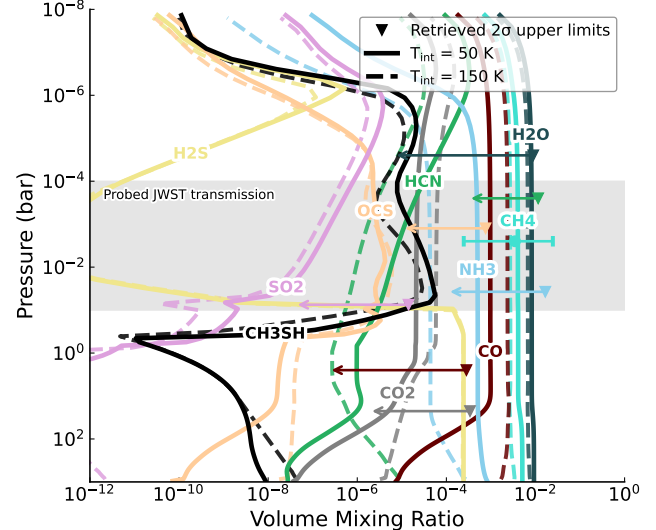


**Figure 10.** Predicted photochemical equilibrium abundances in TOI-199 b for  $T_{\text{int}} = 50$  K (solid curves) and  $T_{\text{int}} = 150$  K (dashed curves). Both scenarios assume enhanced metallicity ( $\text{M}/\text{H} = 10$ ). Background gases are omitted for clarity. Colored arrows indicate the retrieved  $\text{CH}_4$  abundance ( $1\sigma$ ) from ExoTR (Table 2), and  $2\sigma$  upper limits of other species, with arrow length representing  $1\sigma$  uncertainty range. The gray shaded region represents the approximate atmospheric pressure range probed via transmission.

licity. At solar metallicity,  $\text{CH}_4$  and  $\text{NH}_3$  remain within the observed uncertainty range, maintaining their spectral dominance. However, the reduced carbon and oxygen content results in substantially lower abundances of CO,  $\text{CO}_2$ , and OCS, strongly decreasing their contributions to the transmission spectrum. While the deep-atmosphere abundance of HCN scales sharply with metallicity, its upper atmosphere abundance is less affected. HCN is primarily controlled by the balance between photochemical losses and vertical mixing, maintaining similar quenched values regardless of metallicity (R. Hu 2021). Metallicity values higher than  $\approx 10$  cause CO and  $\text{CO}_2$  to overtake  $\text{CH}_4$  as main carbon carriers, pushing these species beyond the observed  $2\sigma$  upper limits. Therefore, it is unlikely that TOI-199 b has significantly higher atmospheric metallicity.

Aside from metallicity and internal temperature,  $K_{zz}$  is a key parameter in shaping the composition in the upper atmosphere. In Figure 12, we highlight the resulting photochemical model differences for the nominal  $K_{zz}$  profile against the Jupiter-like case and a uniform profile of  $10^6 \text{ cm}^2 \text{ s}^{-1}$ . The comparison is shown for  $\text{M}/\text{H} = 10$  with  $T_{\text{int}} = 50$  K.

Due to its uniform abundance, which is mostly dictated by the thermochemical equilibrium in the probed region of the atmosphere, the observability of  $\text{CH}_4$  is

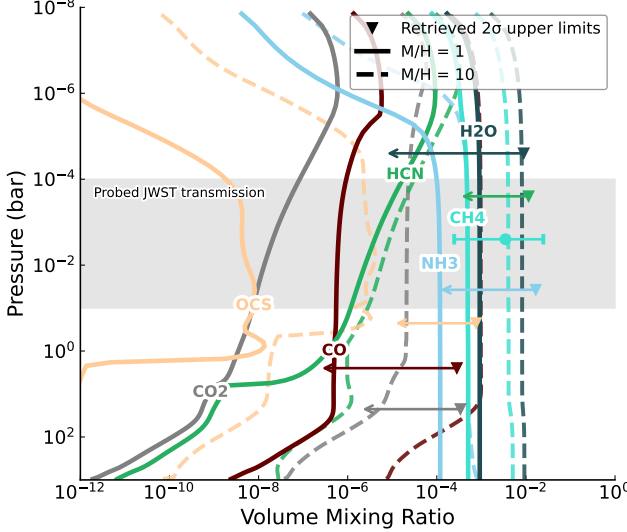


**Figure 11.** Same as Fig. 10, but showing the effect of metallicity. Solar metallicity ( $M/H = 1$ , solid curves) and enhanced metallicity ( $M/H = 10$ , dashed curves) scenarios are compared, both assuming a solar C/O ratio of 0.59 and  $T_{\text{int}} = 50 \text{ K}$ .

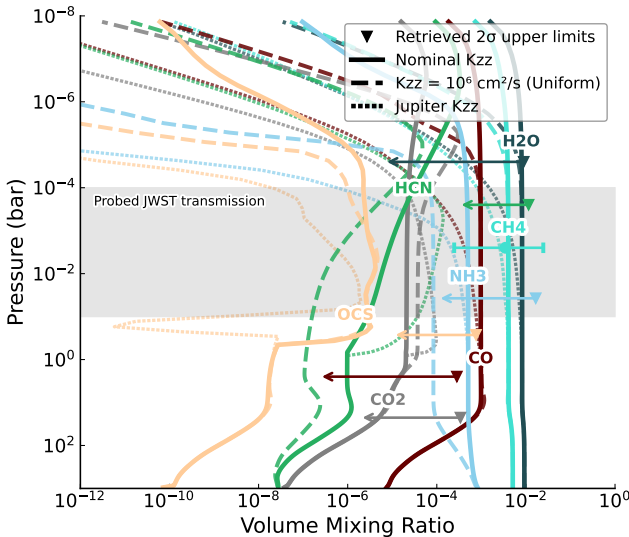


**Figure 12.** Same as Fig. 10, but showing the effect of different eddy diffusion ( $K_{zz}$ ) profiles. Solid curves use the nominal  $K_{zz}$  from Fig. 9, while dashed curves correspond to a uniform  $K_{zz} = 10^6 \text{ cm}^2 \text{ s}^{-1}$  case. Dotted curves correspond to a Jupiter-like  $K_{zz}$  profile. All models are shown for enhanced metallicity ( $M/H = 10$ ) and  $T_{\text{int}} = 50 \text{ K}$ .

only slightly affected by vertical mixing. At  $K_{zz} = 10^6 \text{ cm}^2 \text{ s}^{-1}$  and below, its volume mixing ratio in the upper atmosphere begins to diminish due to increased photodissociation, but the reduction is typically insufficient to affect the transmission spectrum. For the model using a Jupiter-like  $K_{zz}$ , this effect is more substan-

tial. We see a reduced  $\text{CH}_4$  abundance all the way to  $P = 10^{-1}$  bar, which results in its transmission radius being slightly lowered. Similar trends are observed for  $\text{H}_2\text{O}$ .

For species that are non-uniform in the deep atmosphere under thermal equilibrium, such as  $\text{NH}_3$  or  $\text{CO}$ , the vertical mixing strength determines the quenching pressure, which severely affects the abundance in the upper atmosphere. For  $\text{NH}_3$ , the quenching pressure is approximately 10 bar. At uniform  $K_{zz} = 10^6 \text{ cm}^2 \text{ s}^{-1}$ , its volume mixing ratio drops by nearly an order of magnitude, which is sufficient to decrease its opacity to the point where it becomes undetectable, allowing  $\text{H}_2\text{O}$  to dominate the wavelength region. The adopted deep-atmosphere  $K_{zz} = 10^8 \text{ cm}^2 \text{ s}^{-1}$ , which is also assumed in the Jupiter-like cases, allows  $\text{NH}_3$  to sustain an observable abundance.

$\text{HCN}$  formation depends heavily on the supply of atomic nitrogen. In temperate planetary atmospheres, the photochemical formation of  $\text{HCN}$  is enabled by the availability of  $\text{NH}_3$  for photolysis and the presence of methyl radicals (R. Hu 2021). High-energy dissociation of  $\text{N}_2$  can also provide nitrogen for  $\text{HCN}$  formation (e.g., V. Vuitton et al. 2019). In the deep atmosphere,  $\text{HCN}$  is also produced thermochemically and its abundance depends heavily on the quench pressure (J. I. Moses et al. 2010). Additionally, higher internal temperatures disfavor  $\text{NH}_3$  formation, which enhances  $\text{HCN}$  production in the deep atmosphere while reducing its abundance in the observable upper layers due to the decreased nitrogen supply.

For an  $M/H = 10$  atmosphere with nominal internal temperature (50 K), we find that its average upper atmosphere VMR drops by nearly an order of magnitude (from  $\approx 10^{-5}$  to  $\approx 10^{-6}$  VMR) when comparing the nominal  $K_{zz}$  profile and uniform  $K_{zz} = 10^8 \text{ cm}^2 \text{ s}^{-1}$  models. When  $K_{zz}$  is reduced further to  $10^6 \text{ cm}^2 \text{ s}^{-1}$ , the abundance of  $\text{HCN}$  is similarly reduced by nearly an order of magnitude to  $\approx 10^{-7}$ .<sup>15</sup> When  $K_{zz}$  is reduced even further to  $10^4 \text{ cm}^2 \text{ s}^{-1}$ , the abundance of  $\text{HCN}$  does not diminish but instead increases. This is a direct consequence of the photochemically-dominated region shifting deeper into the atmosphere, where dissociation of  $\text{NH}_3$  and  $\text{N}_2$  creates ample supply of atomic nitrogen for  $\text{HCN}$  formation. This effectively indicates that there is a  $K_{zz}$  transition point where  $\text{HCN}$  can overtake  $\text{NH}_3$  as the most abundant nitrogen carrier besides

<sup>15</sup> For other major atmospheric components, such as  $\text{CH}_4$ ,  $\text{H}_2\text{O}$ ,  $\text{NH}_3$ ,  $\text{CO}$ ,  $\text{CO}_2$ , or  $\text{N}_2$ , models with the nominal  $K_{zz}$  profile and a uniform  $K_{zz} = 10^8 \text{ cm}^2 \text{ s}^{-1}$  result in nearly identical abundance profiles and are therefore interchangeable.

$\text{N}_2$ . This effect is more pronounced for the Jupiter-like case, where efficient mixing outside of the convective regions allows HCN to reach  $\approx 10^{-4}$  VMR, bringing its  $3.0 \mu\text{m}$  spectral feature on par with  $\text{NH}_3$ , which would allow both species to be detectable at moderate-to-high spectral resolution.

In terms of observability, sulfur-containing species are less affected by the strength of vertical mixing. When  $K_{zz}$  is reduced to a uniform  $10^6 \text{ cm}^2 \text{ s}^{-1}$  value from the nominal case, increased photochemical dissociation diminishes OCS in the upper atmosphere but slightly increases its abundance at  $P \approx 10^{-2}$  bar, enhancing its  $4.8 \mu\text{m}$  feature. Further reducing  $K_{zz}$  (Jupiter-like profile or similarly a uniform  $10^4 \text{ cm}^2 \text{ s}^{-1}$  model) severely diminishes OCS, though its opacity contribution remains substantial. While not displayed, both  $\text{SO}_2$  and  $\text{CH}_3\text{SH}$  show similar sensitivity to increased photochemical dominance.

### 4.3. Model spectra

Figure 13 shows the resulting transmission spectra of our forward models, comparing several cases that highlight differences in spectral features caused by metallicity or vertical mixing strength. Models labeled  $\text{M}/\text{H} = 10$ ,  $\text{M}/\text{H} = 1$ , Jupiter  $K_{zz}$ , and  $T_{\text{int}} = 150 \text{ K}$  use their respective  $K_{zz}$  profiles from Fig. 9.  $K_{zz} = 10^6 \text{ cm}^2 \text{ s}^{-1}$  uses a uniform  $K_{zz}$  value and a metallicity of  $\text{M}/\text{H} = 10$ . All models and the overlaid NIRSpec data are binned to a resolution of  $\lambda/\Delta\lambda = 100$ , down from the native  $\lambda/\Delta\lambda = 1000$  used for  $\chi^2$  calculations. All spectra are offset to match the observed transit radius, minimizing  $\chi^2$ . Numerical values are tabulated in Table 4. The  $\chi^2$  values are presented in reduced form where the degrees of freedom equal the number of data points at full native resolution.

For the  $\text{M}/\text{H} = 10$  with  $T_{\text{int}} = 50 \text{ K}$  transmission spectrum (teal curve), the spectral shape is determined by contributions from  $\text{CH}_4$ ,  $\text{NH}_3$ ,  $\text{CO}$ ,  $\text{CO}_2$ , and OCS opacities, with individual contributions shown by solid shaded regions. For each species, the colored label denotes where the opacity peaks. Spectral features of  $\text{H}_2\text{O}$ , HCN, and other minor species contribute little to the observed planetary radius. Most of the atmosphere becomes opaque at pressures within an order of magnitude of  $10^{-2}$  bar; however, the strongest  $\text{CH}_4$  absorption feature ( $3.4 \mu\text{m}$ ) becomes opaque at  $\approx 10^{-4}$  bar.

Reducing the metallicity to solar (gray curve) preserves the  $\text{NH}_3$  and  $\text{CH}_4$  features. However, contributions from CO and OCS become negligible, with only  $\text{CO}_2$  at  $4.2 \mu\text{m}$  slightly increasing the transit radius at longer wavelengths.

At an internal temperature of  $150 \text{ K}$  (purple spectrum), the  $\text{NH}_3$  absorption band at  $3.0 \mu\text{m}$  is heavily diminished. Despite larger HCN VMR in the deep atmosphere, its transmission feature at  $3.0 \mu\text{m}$  remains hidden by the  $\text{H}_2\text{O}$  continuum. In contrast, higher abundances of  $\text{CO}$ ,  $\text{CO}_2$ , and OCS, further increase the transmission radius between  $4.2 - 5.1 \mu\text{m}$ , a case disfavored by the NIRSpec data.

The spectral shape is also affected by the  $K_{zz}$  profile. While transitioning from the nominal  $K_{zz}$  profiles to a uniform  $10^8 \text{ cm}^2 \text{ s}^{-1}$  does not result in significant changes, reducing  $K_{zz}$  further does. At  $10^6$  and lower  $K_{zz}$  values (yellow spectrum), increased photochemical dissociation dominance in the upper atmosphere severely reduces  $\text{NH}_3$  abundance, resulting in a strongly diminished  $3.0 \mu\text{m}$  band. Mixing strength also slightly affects the  $\text{CO}_2$  transmission radius. Decreasing  $K_{zz}$  reduces  $\text{CO}_2$  quenching, increasing its abundance. At  $10^6 \text{ cm}^2 \text{ s}^{-1}$ , photochemically produced  $\text{CO}_2$  peaks at observable pressures, making its opacity more dominant. Neighboring CO and OCS opacities are only slightly affected by  $K_{zz}$  variance.

For the model using the Jupiter-like  $K_{zz}$  profile, we see similar, photochemically-induced changes. The individual opacity contributions for this case are marked in dashed shaded regions. More  $\text{NH}_3$  is converted to HCN, resulting in its  $3.0 \mu\text{m}$  band nearly overtaking  $\text{NH}_3$ . Figure 14 displays a zoomed-in, increased resolution comparison between  $\text{NH}_3$  and HCN opacities for the Jupiter-like case. Other species, such as  $\text{CH}_4$ ,  $\text{H}_2\text{O}$ , CO, and OCS are slightly diminished, which results in more  $\text{CO}_2$  being photochemically produced, increasing the transmission radius at  $4.3 \mu\text{m}$ .

Due to the lower-than-expected precision in this program, all of our presented models align closely in  $\chi^2$  (shown in Table 4) and can reasonably explain the atmospheric composition. The best fitting models from our set are the cases with the Jupiter-like  $K_{zz}$  and a uniform  $K_{zz} = 10^8 \text{ cm}^2 \text{ s}^{-1}$  profile, which have enhanced metallicity ( $\text{M}/\text{H} = 10$ ). However, these models almost identically align with cases where the nominal  $K_{zz}$  profiles are used. Although not shown, we find that increasing the metallicity further beyond  $\text{M}/\text{H} = 10$  significantly increases the  $\text{CO}_2$  and CO features, which results in a worse fit, similar to the effect of increased internal temperature.

## 5. TTV ANALYSIS

Strong transit timing variations (TTVs) were detected in the TOI-199 system by M. J. Hobson et al. (2023), who performed a joint analysis between TTV and radial velocity data (RV) obtained by TESS and sev-

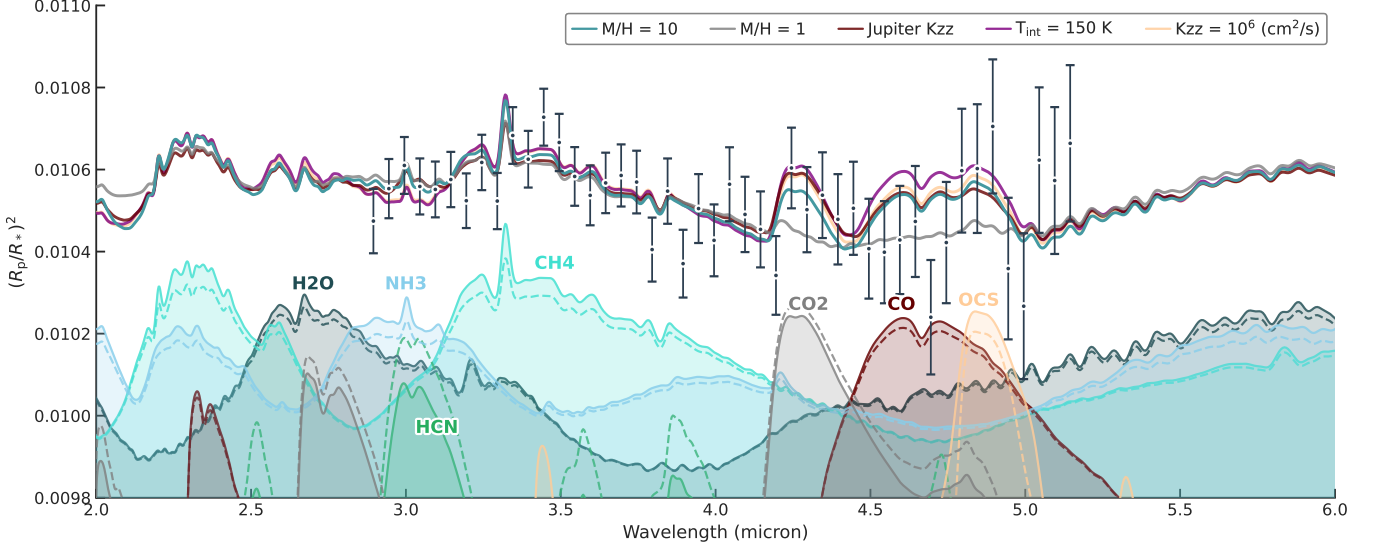


**Figure 13.** Model transmission spectra comparison for TOI-199 b. The teal spectrum represents an enhanced metallicity case ( $M/H = 10$ ) using the nominal  $K_{zz}$  profile. For enhanced metallicity, we also show spectra with a Jupiter-like  $K_{zz}$  profile (red), increased internal temperature (purple), and a uniform  $K_{zz}$  value of  $10^6 \text{ cm}^2 \text{ s}^{-1}$  (orange). Additionally, the solar metallicity spectrum is shown in gray. Individual opacity contributions of the  $M/H = 10$  model are shown via solid shaded regions with corresponding species labels. Individual contributions in dashed represent the Jupiter-like case. NIRSpec data are shown for the fiducial Eureka! reduction binned at  $\lambda/\Delta\lambda = 100$  for visualization.

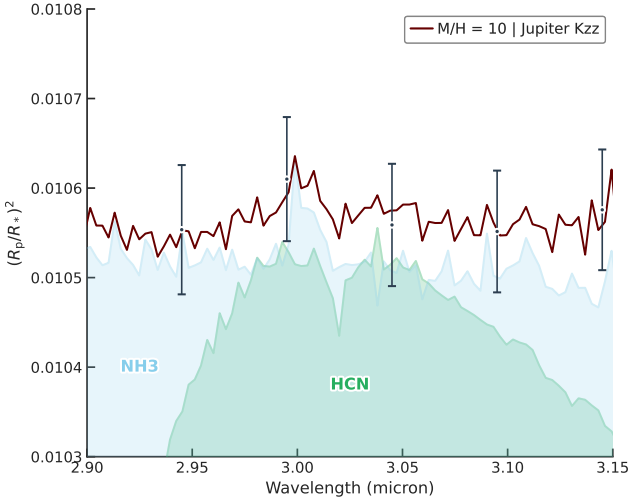


**Figure 14.** Comparison of  $\text{NH}_3$  and  $\text{HCN}$  opacity contributions at  $\lambda/\Delta\lambda = 1000$  for a model spectrum under enhanced metallicity conditions using a Jupiter-like  $K_{zz}$  profile (zoomed-in view from Figure 13). Shaded regions indicate the respective opacity contributions of these nitrogen-bearing species.

eral ground-based observatories to obtain precise constraints on the planetary and orbital parameters. This TTV+RV analysis revealed TTVs with a peak-to-peak amplitude around 60 minutes for TOI-199 b, and characterized a non-transiting planet with an orbital period of  $\sim 274$  days and mass of  $\sim 0.28M_J$ , placing it in the conservative habitable zone. The TOI-199 system is rel-

Model	$\chi^2/\text{dof}$
$M/H = 1$	
Nominal $K_{zz}$	1.0456
$K_{zz} = 10^4 (\text{cm}^2/\text{s})$	1.0457
$K_{zz} = 10^6 (\text{cm}^2/\text{s})$	1.0456
$K_{zz} = 10^8 (\text{cm}^2/\text{s})$	1.0456
$M/H = 10$	
Nominal $K_{zz}$	1.0452
Nominal $K_{zz}$ , $T_{\text{int}} = 150 \text{ K}$	1.0458
Jupiter $K_{zz}$	1.0451
$K_{zz} = 10^4 (\text{cm}^2/\text{s})$	1.0457
$K_{zz} = 10^6 (\text{cm}^2/\text{s})$	1.0459
$K_{zz} = 10^8 (\text{cm}^2/\text{s})$	1.0451

**Table 4.** Summary of  $\chi^2/\text{dof}$  for forward models with different metallicity and  $K_{zz}$  profiles. The  $\chi^2$  values were calculated by comparing native-resolution NIRSpec data to model spectra computed at  $\lambda/\Delta\lambda = 1000$ . The degrees of freedom were taken to be equal to the number of data points.

atively uncommon in that it exhibits strong TTVs, but the two known planets are not near any first- or second-order orbital resonances, which are typically responsible for causing observed TTVs (e.g., Y. Lithwick et al. 2012; T. Holczer et al. 2016). In the case of TOI-199, the two massive planets on eccentric and close-in ( $< 1 \text{ AU}$ ) orbits dynamically perturb each other enough to cause large TTVs without proximity to resonance, which leads

to TTVs that do not exhibit the typical sinusoidal pattern (e.g., E. B. Ford et al. 2012; K. M. Deck & E. Agol 2016, see also Figure 15).

Since the original publication of TTVs in the TOI-199 system in M. J. Hobson et al. (2023), three more transits of TOI-199 b have been observed in subsequent TESS sectors, including one additional transit prior to our scheduled JWST transit observation. We extracted transit times for TOI-199 b from TESS sectors 67, 87 and 94, using the same procedure as described in M. Greklek-McKeon et al. (2025b). In brief, this involved constructing a TESS photometric model using the `exoplanet` package (D. Foreman-Mackey 2018) for the transit lightcurve component, and a Matern-3/2 Gaussian Process (GP) kernel from `celerite2` (D. Foreman-Mackey et al. 2017) to model out-of-transit stellar variability. Our transit model includes parameters for the stellar radius  $R_*$ , impact parameter  $b$ , scaled semimajor axis  $a/R_*$ , planet-to-star radius ratio  $R_p/R_*$ , and individual transit mid-center times to account for TTVs. The GP model includes a mean offset parameter  $\mu$  and hyperparameters  $\sigma$  and  $\rho$  corresponding to the amplitude and timescale of quasiperiodic oscillations, along with an error scaling term added in quadrature to the TESS flux errors. We fixed the planetary eccentricities to zero in the transit fit, as in M. J. Hobson et al. (2023), since the corresponding effect on the transit lightcurve shape is negligible. We also fixed the quadratic limb-darkening parameters  $u_1 = 0.466$  and  $u_2 = 0.117$ , as predicted by the `ldtk` package (H. Parviainen & S. Aigrain 2015) using the stellar temperature, [Fe/H], and log g values reported in M. J. Hobson et al. (2023). We placed Gaussian priors on  $R_*$ ,  $b$ ,  $a/R_*$ , and  $R_p/R_*$  using the values reported in Tables 2 and 3 of M. J. Hobson et al. (2023), and placed a uniform prior on individual transit times  $\pm 12$  hours from the transit time predicted from the M. J. Hobson et al. (2023) ephemeris. We used the PyMC3 package (J. Salvatier et al. 2016) to sample the posterior distribution of our model with four parallel chains run with 2000 burn-in steps and 2000 posterior sample draws. We confirmed that the chains evolved until the Gelman–Rubin statistic values are  $<1.01$  for all parameters, and that the transit mid-time posteriors are unimodal and normally distributed. The transit times from sectors 67, 87, and 94, along with the best-fit JWST transit time, and predicted transit times through December 31, 2040, are listed in Table 5.

Using the new TOI-199 b transit times, we performed an updated TTV fit following the procedure of M. Greklek-McKeon et al. (2025b). This involved using the TTVFast package (K. M. Deck & E. Agol 2016) to model

the observed transit times listed in Table 5. The modeled transit times are a function of the planetary masses and orbital elements relative to a reference epoch at the TTV model start time, which we chose to be 1256.14 (BJD–2 457 000) to match the simulation start time of M. J. Hobson et al. (2023). This simulation start time is close to one orbital period before the first observed transit of TOI-199 b, which can make TTV model convergence more difficult due to slight changes in the orbital period parameter for TOI-199 b altering the total number of transit events within the simulation time period, but we use this start time regardless for consistency with the M. J. Hobson et al. (2023) model.

In our TTV modeling, we fixed the planetary orbital inclinations to  $90^\circ$  and the stellar mass to  $0.936 M_\odot$ , as in the original TTV analysis of M. J. Hobson et al. (2023). Our TTV model has 10 free parameters in total, including: the planet-to-star mass ratios, average Keplerian orbital periods over the simulation period, initial mean anomalies ( $M_0$ ) re-parameterized as the time of first transit ( $T_0$ ), and the planetary eccentricities ( $e$ ) and longitudes of periastron ( $\omega$ ). We re-parameterized the latter two quantities as  $\sqrt{e} \cos(\omega)$  and  $\sqrt{e} \sin(\omega)$  to mitigate the degeneracy between  $e$  and  $\omega$  in our fits while retaining an effective uniform prior on  $e$ , as recommended by (J. Eastman et al. 2013). The orbital periods, mean anomalies, eccentricities, and longitudes of periastron are osculating orbital elements defined at the TTV model start time. We fit this model to the data using the MCMC ensemble sampler `emcee` (D. Foreman-Mackey et al. 2013), and chose wide uniform priors for all parameters (see Table 6) except the mass of TOI-199 b, for which we use a Gaussian prior derived from the independent RV mass constraint of M. J. Hobson et al. (2023), which is scaled from the RV semi-amplitude constraint.

We performed our TTV fit including the original transit times published in M. J. Hobson et al. (2023), the JWST transit time, and additional new TESS data from sectors 67, 87 and 94. The same TOI-199 b transit observed by JWST was also observed by TESS in sector 87, so we used the error-weighted average of these transit times along with its corresponding uncertainty in the TTV model. We initialized this TTV fit with 300 walkers (30 per free parameter) with parameters initialized from the best-fit solution of M. J. Hobson et al. (2023), and ran the MCMC for 50,000 steps, discarding the first 20,000 steps as burn-in and ensuring convergence by verifying that each parameter reached more than 50 autocorrelation lengths in the MCMC. All of our fits to the TESS data used 2-minute cadence data from the Science Processing Operations Center pipeline (SPOC,

J. M. Jenkins et al. 2016), which excluded  $\sim 30\%$  of data that was flagged by the SPOC pipeline for poor data quality, including a potential transit event in sector 90. A more careful photometric extraction from a custom TESS aperture, similar to the technique of M. J. Hobson et al. (2023), may be able to recover an additional transit event for TOI-199 b in future work.

Our updated TTV model including the new JWST data and three additional TESS transits produced results for the masses of TOI-199 b and c consistent within  $2\sigma$  with the results of M. J. Hobson et al. (2023). Our complete TTV model results are listed in Table 6. Our new results improve the precision on the mass of TOI-199 c by approximately 50%, and reduce the uncertainty in the eccentricity by more than a factor of 3 for both planets. Our updated model prefers a larger orbital eccentricity for TOI-199 c ( $0.151 \pm 0.003$ , compared to  $0.096^{+0.008}_{-0.009}$  from M. J. Hobson et al. (2023)), and a slightly larger mean orbital period for TOI-199 c, though still within the conservative habitable zone. Our updated TTV model also yields significantly different  $\omega$  values for both planets, indicating nearly aligned longitudes of periastron for TOI-199 b and c, compared to the nearly anti-aligned  $\omega$  values from the original fit of M. J. Hobson et al. (2023). We see two possible reasons for these changes. The first is simply the addition of new high-precision data improving the accuracy of the TTV fit, especially since there are now 14 total TTV points for a 10 parameter model which makes the TTV solution less poorly constrained than the original 11 point dataset. The second is the difference in parameterization choice for  $e$ ,  $\omega$ , and  $M_0$  which M. J. Hobson et al. (2023) samples directly and uses narrow priors defined by initial test runs, but we re-parameterize these quantities using transformations that reduce the correlations between  $e$ ,  $\omega$ , and  $M_0$  and avoid convergence issues for circular parameters as suggested by previous TTV model comparisons (e.g., J. Eastman et al. 2013; E. Agol et al. 2021; M. Greklek-McKeon et al. 2025a), and we use wide uniform priors with one MCMC sampling until convergence is reached.

The eccentricities of both TOI-199 planets are not large enough to affect their transit shape profile as described in M. J. Hobson et al. (2023), but precise constraints on their  $e$  and  $\omega$  values might be relevant for future eclipse observations of TOI-199 b. Given the shift in best-fit  $e$  and  $\omega$  values when increasing the total data volume from 11 to 14 transits, these best-fit values may still change when more data are available. At the time of this writing, TESS is scheduled to re-observe the TOI-199 system in September, October, and December of 2025, in sectors 96, 97, and 98, respectively. New TTV

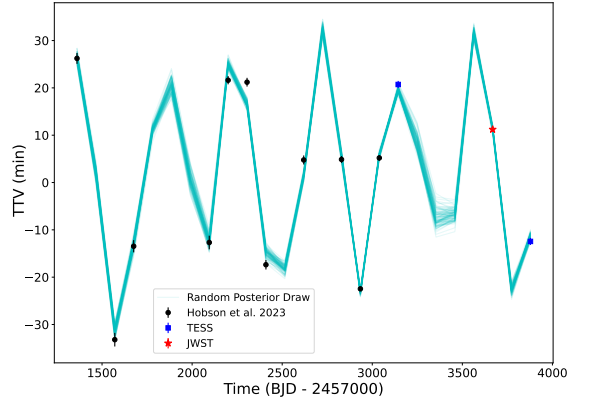


**Figure 15.** Observed TTVs for TOI-199 b from the M. J. Hobson et al. (2023) discovery paper (black points) and new data from JWST (red star) and TESS sectors 67, 87, and 94 (blue squares), along with 100 random draws from the best-fit TTV model (blue lines).

fits with additional transits from these sectors may be able to further refine the mass of TOI-199 c and the orbital parameters for both planets. We list the predicted transit times through December 31, 2040 from our best-fit TTV model in Table 5 to aid in planning future observations of this system.

## 6. DISCUSSION AND CONCLUSIONS

### 6.1. Atmospheric chemistry

TOI-199 b occupies a temperature regime that bridges the well-studied populations of hot Jupiters and solar system giants, allowing us to probe distinctive atmospheric chemistry not observed in either extreme. Unlike in hot Jupiters, where thermal chemistry favors CO/CO<sub>2</sub> over CH<sub>4</sub> and NH<sub>3</sub> is largely dissociated, or cooler giants, where CH<sub>4</sub> and NH<sub>3</sub> are stable, the chemical composition of TOI-199 b reflects a delicate balance between photochemical processes and the strength of vertical mixing.

Taking methane as a proxy for the bulk carbon abundance and thus metallicity (M. Asplund et al. 2009), our constraints from Table 2 correspond to an atmospheric metallicity of C/H =  $13^{+78}_{-12} \times$  solar (or [C/H] =  $1.11^{+0.85}_{-1.15} \times$  solar). However, we consider the high end of this range (i.e.,  $\gtrsim 50 \times$  solar) to be disfavored because our photochemical models predict that at high metallicity, CO would overtake CH<sub>4</sub> as the dominant carbon carrier, which is inconsistent with our measured upper limits on CO and CO<sub>2</sub>. By identical reasoning based on the CO upper limit, our models also disfavor internal temperatures much larger than 50 K.

**Table 5.** Transit Times for TOI-199 b

Transit Time (BJD – 2 457 000)	Source
1361.0283 <sup>+0.0008</sup> <sub>-0.0008</sub>	H23
1465.8841 <sup>+0.0002</sup> <sub>-0.0002</sub>	Predicted
1570.7320 <sup>+0.0010</sup> <sub>-0.0010</sub>	H23
1675.6182 <sup>+0.0009</sup> <sub>-0.0009</sub>	H23
1780.5078 <sup>+0.0009</sup> <sub>-0.0011</sub>	Predicted
1885.3868 <sup>+0.0020</sup> <sub>-0.0026</sub>	Predicted
1990.2454 <sup>+0.0019</sup> <sub>-0.0025</sub>	Predicted
2095.1087 <sup>+0.0010</sup> <sub>-0.0010</sub>	H23
2200.0050 <sup>+0.0006</sup> <sub>-0.0006</sub>	H23
2304.8772 <sup>+0.0006</sup> <sub>-0.0006</sub>	H23
2409.7229 <sup>+0.0007</sup> <sub>-0.0007</sub>	H23
2514.5948 <sup>+0.0051</sup> <sub>-0.0059</sub>	Predicted
2619.4833 <sup>+0.0007</sup> <sub>-0.0007</sub>	H23
2724.3750 <sup>+0.0040</sup> <sub>-0.0050</sub>	Predicted
2829.2283 <sup>+0.0005</sup> <sub>-0.0005</sub>	H23
2934.0818 <sup>+0.0003</sup> <sub>-0.0003</sub>	H23
3038.9735 <sup>+0.0004</sup> <sub>-0.0004</sub>	H23
3143.8568 <sup>+0.0005</sup> <sub>-0.0005</sub>	TESS Sector 67
3248.7207 <sup>+0.0083</sup> <sub>-0.0099</sub>	Predicted
3353.5820 <sup>+0.0086</sup> <sub>-0.0105</sub>	Predicted
3458.4552 <sup>+0.0073</sup> <sub>-0.0091</sub>	Predicted
3563.3545 <sup>+0.0064</sup> <sub>-0.0083</sub>	Predicted
3668.2126 <sup>+0.0003</sup> <sub>-0.0003</sub>	JWST & TESS Sector 87
3773.0616 <sup>+0.0099</sup> <sub>-0.0116</sub>	Predicted
3877.9412 <sup>+0.0005</sup> <sub>-0.0005</sub>	TESS Sector 94
3982.8322 <sup>+0.0082</sup> <sub>-0.0102</sub>	Predicted
4087.7172 <sup>+0.0099</sup> <sub>-0.0125</sub>	Predicted
4192.5741 <sup>+0.0094</sup> <sub>-0.0119</sub>	Predicted
4297.4333 <sup>+0.0085</sup> <sub>-0.0107</sub>	Predicted
...	...

NOTE—H23 is M. J. Hobson et al. (2023). This table is truncated for brevity. The full table including predictions of transit times through December 31, 2040 UTC is available in machine-readable form.

Unlike in cooler gas giants, H<sub>2</sub>O in the atmosphere of TOI-199 b is expected to be retained in the gaseous phase. Although we lack a direct detection, our H<sub>2</sub>O upper limit constraint is within  $1\sigma$  of the CH<sub>4</sub> abundance. Since H<sub>2</sub>O is likely the dominant oxygen carrier in the atmosphere, a measured CH<sub>4</sub>/H<sub>2</sub>O ratio could provide precise constraints on the atmospheric C/O ratio.

The temperate regime of TOI-199 b makes its nitrogen chemistry especially sensitive to ongoing disequilibrium processes. In thermal equilibrium, the dominant nitrogen carrier is predicted to be NH<sub>3</sub>, but with TOI-199 b's insolation, strong UV irradiation drives active

**Table 6.** Prior and posterior distributions from updated TTV modeling including new TESS and JWST data.

Parameter	Prior	Posterior
$M_b$ ( $M_J$ )	$\mathcal{N}(0.169, 0.025)$	$0.170 \pm 0.020$
$M_c$ ( $M_J$ )	$\mathcal{U}(0.0, 5.0)$	$0.261 \pm 0.005$
$P_b$ (days)*	$\mathcal{U}(103.8540, 105.8540)$	$104.869 \pm 0.001$
$P_c$ (days)*	$\mathcal{U}(268.690, 278.69)$	$274.769^{+0.144}_{-0.141}$
$\sqrt{e_b} \cos(\omega_b)$	$\mathcal{U}(-0.7, 0.7)$	$0.136 \pm 0.012$
$\sqrt{e_c} \cos(\omega_c)$	$\mathcal{U}(-0.7, 0.7)$	$0.135 \pm 0.013$
$\sqrt{e_b} \sin(\omega_b)$	$\mathcal{U}(-0.7, 0.7)$	$0.294 \pm 0.008$
$\sqrt{e_c} \sin(\omega_c)$	$\mathcal{U}(-0.7, 0.7)$	$0.364 \pm 0.007$
$e_b$	Derived	$0.105 \pm 0.003$
$e_c$	Derived	$0.151 \pm 0.003$
$\omega_b$	Derived	$65.1 \pm 2.3$
$\omega_c$	Derived	$69.7 \pm 2.1$
$T_{0b}$ (BJD – 2 458 300) <sup>†</sup>	$\mathcal{U}(8.5683, 113.3683)$	$60.999 \pm 0.001$
$T_{0c}$ (BJD – 2 458 300) <sup>†</sup>	$\mathcal{U}(7.43, 281.03)$	$160.741^{+0.685}_{-0.679}$

$\mathcal{U}(a, b)$  is the uniform distribution between values  $a$  and  $b$ .  $\mathcal{N}(a, b)$  is a Gaussian distribution with mean  $a$  and standard deviation  $b$ . The posterior values are reported as the median, with uncertainties given by the 16<sup>th</sup> and 84<sup>th</sup> percentiles.

\*We caution that the period values in this table should never be used to predict future transits in the TOI-199 system. These are approximations of the mean orbital period during the TTV simulation window. Using the period and  $T_0$  values listed here to predict transits beyond the simulation window can result in errors much larger than the TTV amplitude shown in Figure 15. For transit timing predictions through 2040, see Table 5.

<sup>†</sup>The  $T_0$  times listed here are a re-parameterization of the osculating mean anomaly ( $M_0$ ) at the starting time of the simulation (BJD 2 458 262.350), and do not represent true transit times.

photodissociation of both NH<sub>3</sub> and N<sub>2</sub>, supplying nitrogen for HCN formation. This is in contrast to the Jovian atmosphere, where such photochemical processes result in formation of hydrocarbons instead of HCN (G. R. Gladstone et al. 1996; J. Moses et al. 2005; R. Hu 2021). The strength of vertical mixing determines the relative importance of photochemistry: efficient vertical mixing in the deep atmosphere quenches NH<sub>3</sub> at higher pressures, sharply increasing its abundance throughout the atmosphere. As  $K_{zz}$  in the deep atmosphere is decreased, the quenching moves to lower pressures, reducing NH<sub>3</sub> abundance to its equilibrium minimum. Meanwhile, low  $K_{zz}$  values in the upper atmosphere, typical of solar system giants, allow photochemistry to dominate, potentially leading to HCN replacing NH<sub>3</sub> in observable regions. Complicating this interpretation, increased internal temperatures introduce a degeneracy in the NH<sub>3</sub>/HCN diagnostic. Higher internal temperatures diminish NH<sub>3</sub> formation, resulting in diminished features as those caused by inefficient vertical mixing. Thus, a reduced or absent NH<sub>3</sub> abundance could indi-

cate either weak vertical transport or increased internal temperatures. Breaking this degeneracy requires direct constraints on HCN or major oxygen carriers such as CO or CO<sub>2</sub>.

The NH<sub>3</sub>/HCN ratio directly and precisely traces the efficiency of vertical transport in temperate giant atmospheres, creating a unique diagnostic of atmospheric dynamics. Our model with a Jupiter-like  $K_{zz}$  profile represents an important transition point, where lower  $K_{zz}$  values in the shallow atmosphere could make HCN opacity observable via its 3.0  $\mu\text{m}$  feature.

In addition, TOI-199 b's climate allows OCS to be more abundant than SO<sub>2</sub>. The basic chemical pathway is similar to that described in R. Hu et al. (2025). Sulfur originates from the deep atmosphere in the form of H<sub>2</sub>S, which dissociates into H<sub>2</sub> and S. Atomic sulfur then reacts with CO to form OCS. Subsequently, the CH<sub>3</sub> radical abstracts sulfur from OCS to produce CH<sub>3</sub>S, which acts as a catalyst for the formation of CH<sub>3</sub>SH. Both OCS and CH<sub>3</sub>SH remain stable within the observable region of the atmosphere. Although OCS is not detected through its 4.8  $\mu\text{m}$  feature, our forward model predictions of OCS for enhanced metallicity agree well with the retrieved median and upper limit. OCS detection in TOI-199 b may provide a distinctive chemical fingerprint of temperate gas giants that is not observed in the temperature extremes of either solar system giants or hot Jupiters.

## 6.2. Follow-up observations

High-precision observations will be essential to break the degeneracies between metallicity, C/O ratio, and vertical mixing, yielding crucial insights into the formation history and atmospheric dynamics of TOI-199 b and similar temperate giants.

HST GO program 17605 aimed to measure the transmission spectrum of TOI-199 b with WFC3/G141, targeting CH<sub>4</sub>, NH<sub>3</sub> and H<sub>2</sub>O. However, the HST observation was scheduled based on the period and zero-phase values currently listed on the NASA Exoplanet Archive (M. J. Hobson et al. 2023), without accounting for TTVs, which caused the observation to miss the transit (private communication). We caution against using the period or  $T_0$  values in M. J. Hobson et al. (2023) or in this paper to schedule future transit observations, since that can result in errors much larger than the TTV amplitude. Instead, Table 5 lists predicted transit times through December 31, 2040.

JWST is currently scheduled to observe two additional transits of TOI-199 b to probe the 3–5  $\mu\text{m}$  region (GO 7188, L. Acuna et al. 2025). We have simulated an additional transit of TOI-199 b with NIRSpec/G395M for

two end-member nitrogen scenarios: (i) a Jupiter-like  $K_{zz}$  value with 10× solar metallicity, where HCN could be the main nitrogen carrier, and (ii) a hot Jupiter-like  $K_{zz}$  value, where NH<sub>3</sub> dominates. HCN and NH<sub>3</sub> both absorb near 3.0  $\mu\text{m}$ , making them indistinguishable in the current data and limiting constraints on  $K_{zz}$ . However, assuming no WATA issues, we expect that a single transit observed with NIRSpec/G395M would measure the abundances of NH<sub>3</sub> and HCN with  $\sim 0.2$  dex precision. Such measurements would not only conclusively determine the vertical mixing regime of this planet, but they would also constrain the photochemical production mechanisms of HCN (from its mixing ratio).

Such data would also constrain H<sub>2</sub>O, CH<sub>4</sub>, CO<sub>2</sub>, and CO to  $\sim 0.2$  dex precision. This will enable obtaining a comprehensive picture of the planet's C, N, and O inventories, and therefore precise measurements of the planet's metallicity and the elemental ratios C/O and N/O, which may hold clues to the planet's formation history (K. I. Öberg et al. 2011; D. Turrini et al. 2021; E. Pacetti et al. 2022).

The detection of CH<sub>4</sub> in TOI-199 b is consistent with the emerging trend that temperate ( $T_{\text{eq}} \lesssim 400$  K) low-mean-molecular-weight atmospheres display spectral features in transmission spectroscopy (J. Brande et al. 2023; N. Madhusudhan et al. 2023; B. Benneke et al. 2024), with super-puffs as notable exceptions likely due to high-altitudes hazes and/or circumplanetary rings (M. K. Alam et al. 2022; J. E. Libby-Roberts et al. 2025). However, TOI-199 b is the only planet in this list with a mass comparable to that of Jupiter. Ongoing JWST observations of similar long-period planets will not only test whether this trend extends across the gas giant population (J. Fortney et al. 2023; B. Cassese et al. 2025), but also begin to constrain their vertical mixing and photochemical processes, paving the way for a new era of atmospheric studies of temperate gas giants.

## DATA AVAILABILITY

The JWST data used in this work will be publicly available at the end of the one-year exclusive access period in the Mikulski Archive for Space Telescopes (MAST). The transmission spectra presented in this work are available on Zenodo: [10.5281/zenodo.1765311](https://zenodo.1765311)

## ACKNOWLEDGMENTS

This work is based on observations made with the NASA/ESA/CSA James Webb Space Telescope. The data were obtained from the Mikulski Archive for Space

Telescopes at the Space Telescope Science Institute, which is operated by the Association of Universities for Research in Astronomy, Inc., under NASA contract NAS 5-03127 for JWST. These observations are associated with program #5177. Support for this program was provided by NASA through a grant from the Space Telescope Science Institute under NASA contract NAS

5-03127. Part of this research was carried out at the Jet Propulsion Laboratory, California Institute of Technology, under a contract with the National Aeronautics and Space Administration (80NM0018D0004). Part of the high-performance computing resources used in this investigation were provided by funding from the JPL Information and Technology Solutions Directorate.

## APPENDIX

### A. ATMOSPHERIC RETRIEVALS SUPPLEMENTAL INFORMATION

## REFERENCES

- Acuna, L., Berardo, D., Espinoza-Retamal, J. I., et al. 2025, All you need is Love numbers: simultaneous measurement of the oblateness and atmospheric composition of a warm gas giant,, JWST Proposal. Cycle 4, ID. #7188
- Agol, E., Dorn, C., Grimm, S. L., et al. 2021, PSJ, 2, 1, doi: [10.3847/PSJ/abd022](https://doi.org/10.3847/PSJ/abd022)
- Airapetian, V., Glocer, A., Gronoff, G., Hebrard, E., & Danchi, W. 2016, Nature Geoscience, 9, 452
- Alam, M. K., Kirk, J., Dressing, C. D., et al. 2022, The Astrophysical Journal Letters, 927, L5
- Alderson, L., Wakeford, H. R., Alam, M. K., et al. 2023, Nature, 614, 664
- Ali-Dib, M. 2017, Monthly Notices of the Royal Astronomical Society, 467, 2845
- Asplund, M., Amarsi, A. M., & Grevesse, N. 2021, A&A, 653, A141, doi: [10.1051/0004-6361/202140445](https://doi.org/10.1051/0004-6361/202140445)
- Asplund, M., Grevesse, N., Sauval, A. J., & Scott, P. 2009, ARA&A, 47, 481, doi: [10.1146/annurev.astro.46.060407.145222](https://doi.org/10.1146/annurev.astro.46.060407.145222)
- Barber, R. J., Strange, J. K., Hill, C., et al. 2014, MNRAS, 437, 1828, doi: [10.1093/mnras/stt2011](https://doi.org/10.1093/mnras/stt2011)
- Batalha, N. E., Mandell, A., Pontoppidan, K., et al. 2017, Publications of the Astronomical Society of the Pacific, 129, 064501
- Behr, P. R., France, K., Brown, A., et al. 2023, AJ, 166, 35, doi: [10.3847/1538-3881/acdb70](https://doi.org/10.3847/1538-3881/acdb70)
- Beichman, C. A., Giles, H. A. C., Akeson, R., et al. 2018, AJ, 155, 158, doi: [10.3847/1538-3881/aaaeb6](https://doi.org/10.3847/1538-3881/aaaeb6)
- Bell, T., Ahrer, E.-M., Brande, J., et al. 2022, The Journal of Open Source Software, 7, 4503, doi: [10.21105/joss.04503](https://doi.org/10.21105/joss.04503)
- Bell, T. J., Welbanks, L., Schlawin, E., et al. 2023, Nature, 623, 709, doi: [10.1038/s41586-023-06687-0](https://doi.org/10.1038/s41586-023-06687-0)
- Bello-Arufe, A., Damiano, M., Bennett, K. A., et al. 2025, ApJL, 980, L26, doi: [10.3847/2041-8213/adaf22](https://doi.org/10.3847/2041-8213/adaf22)
- Benneke, B., Roy, P.-A., Coulombe, L.-P., et al. 2024, arXiv e-prints, arXiv:2403.03325, doi: [10.48550/arXiv.2403.03325](https://doi.org/10.48550/arXiv.2403.03325)
- Birkmann, S. M., Ferruit, P., Giardino, G., et al. 2022, A&A, 661, A83, doi: [10.1051/0004-6361/202142592](https://doi.org/10.1051/0004-6361/202142592)
- Bjoraker, G. L., Wong, M. H., de Pater, I., et al. 2018, AJ, 156, 101
- Brande, J., Crossfield, I. J., Kreidberg, L., et al. 2023, arXiv preprint arXiv:2310.07714
- Buchner, J., Georgakakis, A., Nandra, K., et al. 2014, A&A, 564, A125, doi: [10.1051/0004-6361/201322971](https://doi.org/10.1051/0004-6361/201322971)
- Bushouse, H., Eisenhamer, J., Dencheva, N., et al. 2024, JWST Calibration Pipeline, 1.15.1 Zenodo, doi: [10.5281/zenodo.12692459](https://doi.org/10.5281/zenodo.12692459)
- Cassese, B., Kipping, D., Changeat, Q., et al. 2025, arXiv e-prints, arXiv:2511.02067, doi: [10.48550/arXiv.2511.02067](https://doi.org/10.48550/arXiv.2511.02067)
- Chubb, K. L., Rocchetto, M., Yurchenko, S. N., et al. 2021, A&A, 646, A21, doi: [10.1051/0004-6361/202038350](https://doi.org/10.1051/0004-6361/202038350)
- Cridland, A. J., van Dishoeck, E. F., Alessi, M., & Pudritz, R. E. 2019, Astronomy & Astrophysics, 632, A63
- Cridland, A. J., van Dishoeck, E. F., Alessi, M., & Pudritz, R. E. 2020, Astronomy & Astrophysics, 642, A229
- Damiano, M., Bello-Arufe, A., Yang, J., & Hu, R. 2024, ApJL, 968, L22, doi: [10.3847/2041-8213/ad5204](https://doi.org/10.3847/2041-8213/ad5204)
- Deck, K. M., & Agol, E. 2016, ApJ, 821, 96, doi: [10.3847/0004-637X/821/2/96](https://doi.org/10.3847/0004-637X/821/2/96)
- Eastman, J., Gaudi, B. S., & Agol, E. 2013, Publications of the Astronomical Society of the Pacific, 125, 83–112, doi: [10.1086/669497](https://doi.org/10.1086/669497)
- Ehrenreich, D., Lovis, C., Allart, R., et al. 2020, Nature, 580, 597, doi: [10.1038/s41586-020-2107-1](https://doi.org/10.1038/s41586-020-2107-1)

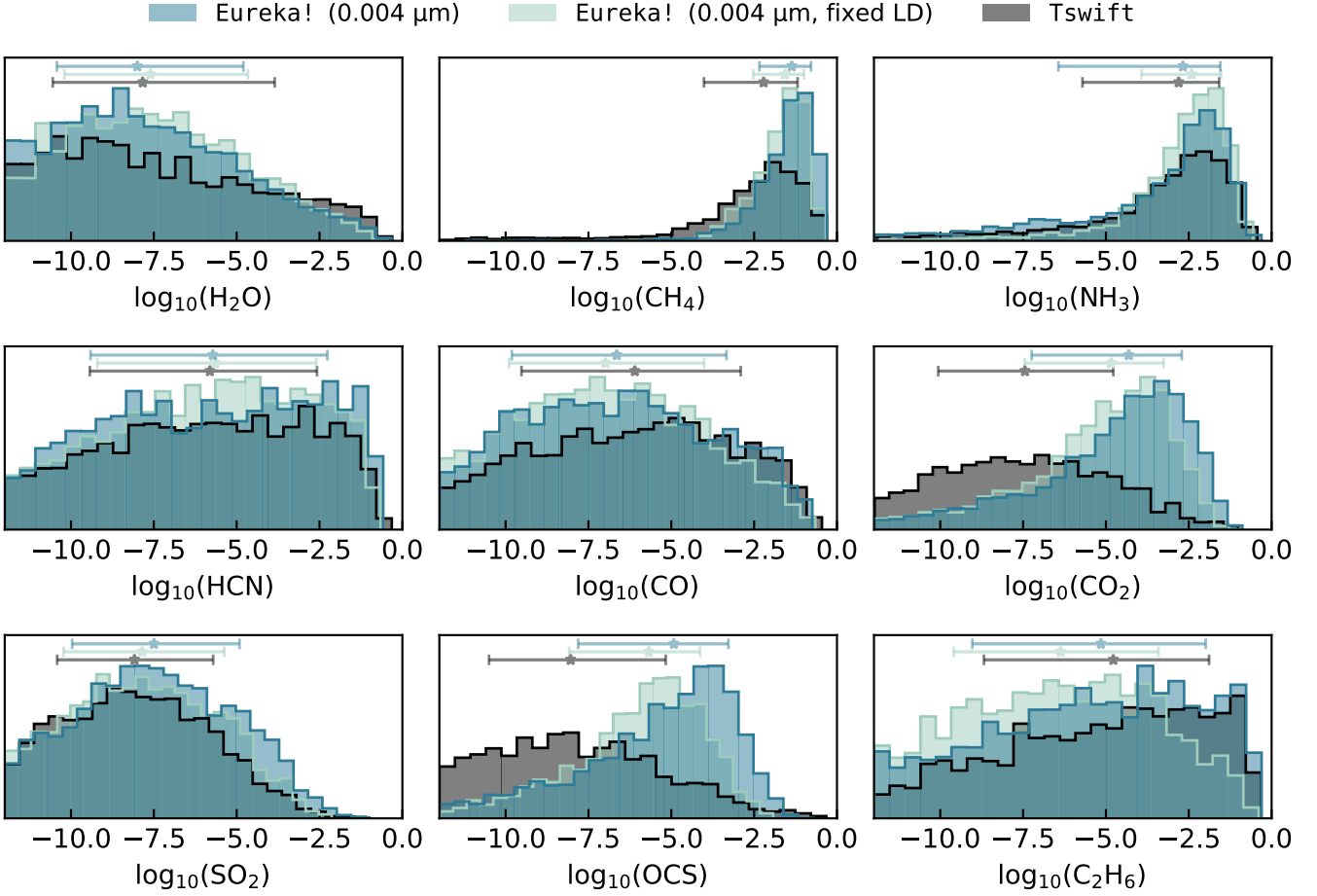


**Figure A1.** Same as Figure 6 but for Aurora.

Espinoza, N., Fortney, J. J., Miguel, Y., Thorngren, D., & Murray-Clay, R. 2017, The Astrophysical Journal Letters, 838, L9

Feinstein, A. D., Radica, M., Welbanks, L., et al. 2023, Nature, 614, 670

Feroz, F., Hobson, M. P., & Bridges, M. 2009, Monthly Notices of the Royal Astronomical Society, 398, 1601, doi: [10.1111/j.1365-2966.2009.14548.x](https://doi.org/10.1111/j.1365-2966.2009.14548.x)

Ford, E. B., Ragozzine, D., Rowe, J. F., et al. 2012, ApJ, 756, 185, doi: [10.1088/0004-637X/756/2/185](https://doi.org/10.1088/0004-637X/756/2/185)

Foreman-Mackey, D. 2018, Research Notes of the American Astronomical Society, 2, 31, doi: [10.3847/2515-5172/aaaf6c](https://doi.org/10.3847/2515-5172/aaaf6c)

Foreman-Mackey, D., Agol, E., Ambikasaran, S., & Angus, R. 2017, AJ, 154, 220, doi: [10.3847/1538-3881/aa9332](https://doi.org/10.3847/1538-3881/aa9332)

Foreman-Mackey, D., Hogg, D. W., Lang, D., & Goodman, J. 2013, PASP, 125, 306, doi: [10.1086/670067](https://doi.org/10.1086/670067)

Fortney, J., Bean, J. L., Fu, G., et al. 2023, C,N,O in a Temperate Jupiter: Bridging the Gap Between Solar-System and Exoplanet Atmospheres,, JWST Proposal. Cycle 2, ID. #3235

Fortney, J. J., Visscher, C., Marley, M. S., et al. 2020, The Astronomical Journal, 160, 288

Fu, G., Espinoza, N., Sing, D. K., et al. 2022, ApJL, 940, L35, doi: [10.3847/2041-8213/ac9977](https://doi.org/10.3847/2041-8213/ac9977)

Fu, G., Welbanks, L., Deming, D., et al. 2024, Nature, 632, 752, doi: [10.1038/s41586-024-07760-y](https://doi.org/10.1038/s41586-024-07760-y)

Gladstone, G. R., Allen, M., & Yung, Y. 1996, Icarus, 119, 1 Gordon, I. E., Rothman, L. S., Hargreaves, R. J., et al. 2022, JQSRT, 277, 107949, doi: [10.1016/j.jqsrt.2021.107949](https://doi.org/10.1016/j.jqsrt.2021.107949)

Graham, R. J., Lichtenberg, T., Boukrouche, R., & Pierrehumbert, R. T. 2021, PSJ, 2, 207, doi: [10.3847/PSJ/ac214c](https://doi.org/10.3847/PSJ/ac214c)

Grant, D., & Wakeford, H. R. 2022, Exo-TiC/ExoTiC-LD: ExoTiC-LD v3.0.0, v3.0.0 Zenodo, doi: [10.5281/zenodo.7437681](https://doi.org/10.5281/zenodo.7437681)

- Grant, D., Lewis, N. K., Wakeford, H. R., et al. 2023, The Astrophysical Journal Letters, 956, L29
- Greklek-McKeon, M., Knutson, H. A., Levine, W. G., et al. 2025a, AJ, 170, 65, doi: [10.3847/1538-3881/addirf2d](https://doi.org/10.3847/1538-3881/addirf2d)
- Greklek-McKeon, M., Vissapragada, S., Knutson, H. A., et al. 2025b, AJ, 169, 292, doi: [10.3847/1538-3881/adc0fe](https://doi.org/10.3847/1538-3881/adc0fe)
- Hargreaves, R. J., Gordon, I. E., Rey, M., et al. 2020, ApJS, 247, 55, doi: [10.3847/1538-4365/ab7a1a](https://doi.org/10.3847/1538-4365/ab7a1a)
- He, C., Radke, M., Moran, S. E., et al. 2024, Nature Astronomy, 8, 182, doi: [10.1038/s41550-023-02140-4](https://doi.org/10.1038/s41550-023-02140-4)
- Heng, K., Malik, M., & Kitzmann, D. 2018, ApJS, 237, 29, doi: [10.3847/1538-4365/aad199](https://doi.org/10.3847/1538-4365/aad199)
- Hess, M., Koepke, P., & Schult, I. 1998, Bulletin of the American Meteorological Society, 79, 831, doi: [10.1175/1520-0477\(1998\)079<0831:OPOAAC>2.0.CO;2](https://doi.org/10.1175/1520-0477(1998)079<0831:OPOAAC>2.0.CO;2)
- Hobbs, R., Shorttle, O., Madhusudhan, N., & Rimmer, P. 2019, Monthly Notices of the Royal Astronomical Society, 487, 2242
- Hobson, M. J., Trifonov, T., Henning, T., et al. 2023, AJ, 166, 201, doi: [10.3847/1538-3881/acfc1d](https://doi.org/10.3847/1538-3881/acfc1d)
- Hobson, M. J., Trifonov, T., Henning, T., et al. 2023, arXiv e-prints, arXiv
- Holczer, T., Mazeh, T., Nachmani, G., et al. 2016, ApJS, 225, 9, doi: [10.3847/0067-0049/225/1/9](https://doi.org/10.3847/0067-0049/225/1/9)
- Hu, R. 2021, The Astrophysical Journal, 921, 27
- Hu, R., Bello-Arufe, A., Zhang, M., et al. 2024, Nature, 630, 609, doi: [10.1038/s41586-024-07432-x](https://doi.org/10.1038/s41586-024-07432-x)
- Hu, R., Bello-Arufe, A., Tokadjian, A., et al. 2025, arXiv e-prints, arXiv:2507.12622, doi: [10.48550/arXiv.2507.12622](https://doi.org/10.48550/arXiv.2507.12622)
- Husser, T. O., Wende-von Berg, S., Dreizler, S., et al. 2013, A&A, 553, A6, doi: [10.1051/0004-6361/201219058](https://doi.org/10.1051/0004-6361/201219058)
- Jakobsen, P., Ferruit, P., Alves de Oliveira, C., et al. 2022, A&A, 661, A80, doi: [10.1051/0004-6361/202142663](https://doi.org/10.1051/0004-6361/202142663)
- Jenkins, J. M., Twicken, J. D., McCauliff, S., et al. 2016, in Society of Photo-Optical Instrumentation Engineers (SPIE) Conference Series, Vol. 9913, Software and Cyberinfrastructure for Astronomy IV, ed. G. Chiozzi & J. C. Guzman, 99133E, doi: [10.1117/12.2233418](https://doi.org/10.1117/12.2233418)
- Kawashima, Y., & Ikoma, M. 2018, The Astrophysical Journal, 853, 7
- Khare, B. N., Sagan, C., Arakawa, E. T., et al. 1984, Icarus, 60, 127, doi: [10.1016/0019-1035\(84\)90142-8](https://doi.org/10.1016/0019-1035(84)90142-8)
- Kipping, D. M. 2013, MNRAS, 435, 2152, doi: [10.1093/mnras/stt1435](https://doi.org/10.1093/mnras/stt1435)
- Knutson, H. A., Charbonneau, D., Allen, L. E., et al. 2007, Nature, 447, 183, doi: [10.1038/nature05782](https://doi.org/10.1038/nature05782)
- Kreidberg, L. 2015, PASP, 127, 1161, doi: [10.1086/683602](https://doi.org/10.1086/683602)
- Lecavelier Des Etangs, A., Pont, F., Vidal-Madjar, A., & Sing, D. 2008, A&A, 481, L83, doi: [10.1051/0004-6361:200809388](https://doi.org/10.1051/0004-6361:200809388)
- Libby-Roberts, J. E., Bello-Arufe, A., Berta-Thompson, Z. K., et al. 2025, arXiv e-prints, arXiv:2505.21358, doi: [10.48550/arXiv.2505.21358](https://doi.org/10.48550/arXiv.2505.21358)
- Lindzen, R. S. 1981, Journal of Geophysical Research: Oceans, 86, 9707
- Line, M. R., & Parmentier, V. 2016, ApJ, 820, 78, doi: [10.3847/0004-637X/820/1/78](https://doi.org/10.3847/0004-637X/820/1/78)
- Line, M. R., Vasisth, G., Chen, P., Angerhausen, D., & Yung, Y. L. 2011, The Astrophysical Journal, 738, 32
- Lithwick, Y., Xie, J., & Wu, Y. 2012, The Astrophysical Journal, 761, 122, doi: [10.1088/0004-637x/761/2/122](https://doi.org/10.1088/0004-637x/761/2/122)
- MacDonald, R. J., & Madhusudhan, N. 2017, MNRAS, 469, 1979, doi: [10.1093/mnras/stx804](https://doi.org/10.1093/mnras/stx804)
- Madhusudhan, N., Sarkar, S., Constantinou, S., et al. 2023, ApJL, 956, L13, doi: [10.3847/2041-8213/acf577](https://doi.org/10.3847/2041-8213/acf577)
- Madhusudhan, N., & Seager, S. 2009, ApJ, 707, 24, doi: [10.1088/0004-637X/707/1/24](https://doi.org/10.1088/0004-637X/707/1/24)
- Magic, Z., Chiavassa, A., Collet, R., & Asplund, M. 2015, A&A, 573, A90, doi: [10.1051/0004-6361/201423804](https://doi.org/10.1051/0004-6361/201423804)
- Mancini, L., Lillo-Box, J., Southworth, J., et al. 2016, A&A, 590, A112, doi: [10.1051/0004-6361/201526357](https://doi.org/10.1051/0004-6361/201526357)
- Mollière, P., Wardenier, J. P., van Boekel, R., et al. 2019, A&A, 627, A67, doi: [10.1051/0004-6361/201935470](https://doi.org/10.1051/0004-6361/201935470)
- Mollière, P., Stolk, T., Lacour, S., et al. 2020, A&A, 640, A131, doi: [10.1051/0004-6361/202038325](https://doi.org/10.1051/0004-6361/202038325)
- Mordasini, C., van Boekel, R., Mollière, P., Henning, T., & Benneke, B. 2016, The Astrophysical Journal, 832, 41
- Moses, J., Fouchet, T., Bézard, B., et al. 2005, Journal of Geophysical Research: Planets, 110
- Moses, J. I., Visscher, C., Keane, T. C., & Sperier, A. 2010, Faraday Discussions, 147, 103, doi: [10.1039/c003954c](https://doi.org/10.1039/c003954c)
- Murgas, F., Chen, G., Pallé, E., Nortmann, L., & Nowak, G. 2019, A&A, 622, A172, doi: [10.1051/0004-6361/201834063](https://doi.org/10.1051/0004-6361/201834063)
- Nixon, M. C., Welbanks, L., McGill, P., & Kempton, E. M. R. 2024, ApJ, 966, 156, doi: [10.3847/1538-4357/ad354e](https://doi.org/10.3847/1538-4357/ad354e)
- Öberg, K. I., Murray-Clay, R., & Bergin, E. A. 2011, The Astrophysical Journal Letters, 743, L16
- Ohno, K., & Fortney, J. J. 2023, The Astrophysical Journal, 946, 18
- Pacetti, E., Turrini, D., Schisano, E., et al. 2022, ApJ, 937, 36, doi: [10.3847/1538-4357/ac8b11](https://doi.org/10.3847/1538-4357/ac8b11)
- Parviainen, H., & Aigrain, S. 2015, Monthly Notices of the Royal Astronomical Society, 453, 3822–3827, doi: [10.1093/mnras/stv1857](https://doi.org/10.1093/mnras/stv1857)

- Richard, C., Gordon, I. E., Rothman, L. S., et al. 2012, JQSRT, 113, 1276, doi: [10.1016/j.jqsrt.2011.11.004](https://doi.org/10.1016/j.jqsrt.2011.11.004)
- Rimmer, P. B., & Rugheimer, S. 2019, Icarus, 329, 124
- Rothman, L. S., Gordon, I. E., Barber, R. J., et al. 2010, JQSRT, 111, 2139, doi: [10.1016/j.jqsrt.2010.05.001](https://doi.org/10.1016/j.jqsrt.2010.05.001)
- Salvatier, J., Wiecki, T. V., & Fonnesbeck, C. 2016, PeerJ Computer Science, 2, e55
- Showman, A. P., Lewis, N. K., & Fortney, J. J. 2015, ApJ, 801, 95, doi: [10.1088/0004-637X/801/2/95](https://doi.org/10.1088/0004-637X/801/2/95)
- Sing, D. K., Fortney, J. J., Nikolov, N., et al. 2016, Nature, 529, 59, doi: [10.1038/nature16068](https://doi.org/10.1038/nature16068)
- Speagle, J. S. 2020, MNRAS, 493, 3132, doi: [10.1093/mnras/staa278](https://doi.org/10.1093/mnras/staa278)
- Tennyson, J., Yurchenko, S. N., Al-Refaie, A. F., et al. 2016, Journal of Molecular Spectroscopy, 327, 73, doi: [10.1016/j.jms.2016.05.002](https://doi.org/10.1016/j.jms.2016.05.002)
- Thorngren, D. P., Sing, D. K., & Mukherjee, S. 2025, arXiv e-prints, arXiv:2510.00169, doi: [10.48550/arXiv.2510.00169](https://doi.org/10.48550/arXiv.2510.00169)
- Tsai, S.-M., Innes, H., Lichtenberg, T., et al. 2021a, The Astrophysical Journal Letters, 922, L27
- Tsai, S.-M., Malik, M., Kitzmann, D., et al. 2021b, The Astrophysical Journal, 923, 264
- Tsai, S.-M., Lee, E. K., Powell, D., et al. 2023, Nature, 617, 483
- Turrini, D., Schisano, E., Fonte, S., et al. 2021, ApJ, 909, 40, doi: [10.3847/1538-4357/abd6e5](https://doi.org/10.3847/1538-4357/abd6e5)
- Underwood, D. S., Tennyson, J., Yurchenko, S. N., et al. 2016, Monthly Notices of the Royal Astronomical Society, 459, 3890, doi: [10.1093/mnras/stw849](https://doi.org/10.1093/mnras/stw849)
- Vuitton, V., Yelle, R., Klippenstein, S., Hörst, S., & Lavvas, P. 2019, Icarus, 324, 120
- Wang, D., Lunine, J. I., & Mousis, O. 2016, Icarus, 276, 21
- Welbanks, L., & Madhusudhan, N. 2019, AJ, 157, 206, doi: [10.3847/1538-3881/ab14de](https://doi.org/10.3847/1538-3881/ab14de)
- Welbanks, L., & Madhusudhan, N. 2021, ApJ, 913, 114, doi: [10.3847/1538-4357/abee94](https://doi.org/10.3847/1538-4357/abee94)
- Welbanks, L., & Madhusudhan, N. 2022, ApJ, 933, 79, doi: [10.3847/1538-4357/ac6df1](https://doi.org/10.3847/1538-4357/ac6df1)
- Welbanks, L., Bell, T. J., Beatty, T. G., et al. 2024, Nature, 630, 836, doi: [10.1038/s41586-024-07514-w](https://doi.org/10.1038/s41586-024-07514-w)
- Welbanks, L., Nixon, M. C., McGill, P., et al. 2025, arXiv e-prints, arXiv:2504.21788, doi: [10.48550/arXiv.2504.21788](https://doi.org/10.48550/arXiv.2504.21788)
- Wilzewski, J. S., Gordon, I. E., Kochanov, R. V., Hill, C., & Rothman, L. S. 2016, JQSRT, 168, 193, doi: <https://doi.org/10.1016/j.jqsrt.2015.09.003>
- Winn, J. N., Holman, M. J., Torres, G., et al. 2008, ApJ, 683, 1076, doi: [10.1086/589737](https://doi.org/10.1086/589737)
- Yang, J. 2025, RMG-generated Chemical Network for H<sub>2</sub>O-rich atmospheres (Yang and Hu, 2024), Zenodo, doi: [10.5281/zenodo.16750016](https://doi.org/10.5281/zenodo.16750016)
- Yang, J., & Hu, R. 2024a, The Astrophysical Journal, 966, 189, doi: [10.3847/1538-4357/ad35c8](https://doi.org/10.3847/1538-4357/ad35c8)
- Yang, J., & Hu, R. 2024b, The Astrophysical Journal Letters, 971, L48, doi: [10.3847/2041-8213/ad6b25](https://doi.org/10.3847/2041-8213/ad6b25)
- Yang, J., Hyder, A., Hu, R., & Lunine, J. I. 2025, arXiv preprint arXiv:2508.05007
- Yu, X., Moses, J. I., Fortney, J. J., & Zhang, X. 2021, The Astrophysical Journal, 914, 38
- Yurchenko, S. N., Barber, R. J., & Tennyson, J. 2011, MNRAS, 413, 1828, doi: [10.1111/j.1365-2966.2011.18261.x](https://doi.org/10.1111/j.1365-2966.2011.18261.x)
- Yurchenko, S. N., & Tennyson, J. 2014, MNRAS, 440, 1649, doi: [10.1093/mnras/stu326](https://doi.org/10.1093/mnras/stu326)
- Zhang, X., & Showman, A. P. 2018, The Astrophysical Journal, 866, 1
- Zilinskas, M., van Buchem, C. P. A., Zieba, S., et al. 2025, A&A, 697, A34, doi: [10.1051/0004-6361/202554062](https://doi.org/10.1051/0004-6361/202554062)